Numerical Analysis of Airfoil Trailing-Edge Noise for Straight and Serrated Edges at Incidence

Romani, G.; Casalino, D.; van der Velden, Wouter

DOI
10.2514/1.J059457

Publication date
2021

Document Version
Accepted author manuscript

Published in
AIAA Journal: devoted to aerospace research and development

Numerical Analysis of Airfoil Trailing-edge Noise for Straight and Serrated Edges at Incidence

Gianluca Romani*, Damiano Casalino†
Delft University of Technology, Kluyverweg 1, 2629HS, Delft, Netherlands

Wouter van der Velden‡
Dassault Systèmes B.V., Utopialaan 25, 5232 CD, 's-Herthogenbosch, Netherlands

The goal of this paper is to perform a detailed analysis of the hydrodynamic near-field and acoustic far-field of a NACA 64-618 airfoil with and without serrations. The impact of serrations is investigated across different airfoil angles of attack and serration flap angles. The natural boundary-layer transition cases 6 and 7 of the AIAA BANC-V Workshop Category 1 are considered as benchmark for the straight edge cases. The numerical simulations are performed using the fully explicit, transient and compressible lattice-Boltzmann equation implemented in the CFD/CAA solver SIMULIA PowerFLOW®. The acoustic far-field is obtained by using the Ffowcs-Williams & Hawkings integral solution applied to the airfoil surface. A mesh resolution study is performed on the straight trailing-edge cases to demonstrate the grid independence of the numerical solution. The numerical results compare favorably against the experimental data. The impact of the serration flap angle on the effectiveness of sawtooth serrations in reducing noise is investigated by considering three different serration flap angles. It is found that the serration flap angle primarily affects the trailing-edge noise reduction through a modification of: (i) the effective angle at which the turbulent structures are convected over the serrated edge; (ii) the convection velocity and spanwise coherence length along the serration; (iii) the intensity of the hydrodynamic wall-pressure fluctuations that are scattered along the serrated edge. The first and last phenomena are expected to play the most important role on the far-field noise reduction.

Nomenclature

b_c = Non-dimensional Corcos' parameter [-]

c = Airfoil chord [m]

C = Cross-spectrum [-]

*PhD Candidate, AWEP Department, G.Romani@tudelft.nl, AIAA member
†Professor of Aeracoustics, AWEP Department, D.Casalino@tudelft.nl, AIAA member
‡Industry Process Expert Specialist, Aerospace & Defense, Wouter.VANDERVELDEN@3ds.com, AIAA member

C_D	=	Sectional drag coefficient [-]
C_L	=	Sectional lift coefficient [-]
C_p	=	Pressure coefficient [-]
C_f	=	Skin friction coefficient [-]
f	=	Frequency [Hz]
h	=	Serration length [m]
l_z	=	Spanwise coherence length [m]
M	=	Mach number [-]
p	=	Fluid pressure [Pa]
p_{rms}	=	Fluid pressure root-mean square [Pa]
R	=	Observer distance [m]
Re	=	Reynolds number [-]
s	=	Airfoil span [m]
St_c	=	Chord-based Strouhal number [-]
t	=	Time [s]
t_s	=	Serration thickness [m]
T	=	Fluid temperature [K]
u, v, w	=	Wall-parallel, wall-normal and spanwise fluid velocity components [m/s]
u_c	=	Convection velocity [m/s]
u_a	=	Slip velocity [m/s]
U	=	Fluid velocity magnitude [m/s]
U_e	=	Edge velocity [m/s]
x, y, z	=	Airfoil reference frame Cartesian coordinates [m]
x_r, y_r, z_r	=	Serration reference frame Cartesian coordinates [m]
y^+	=	Non-dimensional wall-distance in viscous units [-]
α	=	Airfoil angle of attack [deg]
β	=	Serration flap angle [deg]
γ	=	Pressure coherence function [-]
δ	=	Boundary-layer thickness [m]
δ^*	=	Displacement thickness [m]
η	=	Separation distance [m]
θ	=	Observer angle [deg]

Θ = Momentum thickness [m]

λ = Serration wavelength [m]

ρ = Fluid density [kg/m^3]

τ_w = Wall shear-stress [Pa]

ϕ = Cross-spectral density phase [deg]

φ = Near-wall flow direction [deg]

Φ_{aa} = 1/3-octave band far-field sound pressure level [dB]

Φ_{pp} = Wall-pressure power spectral density [dB/Hz]

ω_x = Streamwise vorticity component [1/s]

ζ = Non-dimensional convection velocity parameter [-]

$_\infty$ = Free-stream condition

$'$ = Flow quantity fluctuation

$<>$ = Time-averaged flow quantity

$\bar{}$ = Mean quantity

I. Introduction

Airfoil self-noise, caused by the airfoil interaction with the self-generated flow disturbances, is widely considered as one of the most important sources of aerodynamic noise for applications involving rotating blades, such as helicopter rotors [1, 2], aircraft propellers [3, 4], low-speed fans [5, 6] and wind turbines [7, 8]. Among the different aerodynamic noise mechanisms that can be ascribed to airfoil self-noise [9], the turbulent boundary-layer trailing-edge noise is of primary interest, being the dominant broadband noise contributor for a rotating blade in a homogeneous stationary flow [5, 9]. Trailing-edge noise is the sound associated to the scattering of the turbulent boundary-layer pressure fluctuations at the airfoil trailing-edge. When the boundary-layer pressure waves encounter a surface discontinuity, such as the airfoil trailing-edge, the hydrodynamic turbulent energy is converted into acoustic energy and radiated into the far-field [4, 9].

The rapid expansion of small rotary-wing Unmanned Aerial Vehicles (UAVs) for commercial, scientific or recreational applications, as well as the emergent aviation market of propeller-driven Personal Aerial Vehicles (PAVs) for on-demand aviation services, has recently renewed the interest in accurately predicting and reducing the acoustic signature associated to this type of airfoil self-noise mechanism. For such low-speed rotary-wing configurations, trailing-edge noise can be a significant source of acoustic annoyance, due to the efficient scattering mechanism of the turbulent boundary-layer fluctuations at low Mach numbers [10].

Starting from Howe's analytical studies on serrated trailing-edges [11, 12], several passive noise-mitigation solutions

devoted to reducing the scattering efficiency (and thus eventually the trailing-edge noise) by means of diffraction effects, have been proposed and tested by various authors in the past years [13–20]. Among them, sawtooth trailing-edge serrations represent the most popular ones due to their good compromise in terms of noise reduction and ease of manufacturing. Serrations are widely used for broadband noise reduction of wind turbines nowadays [20] and they are starting to spread to low-speed propeller applications as well [21, 22]. The mechanisms behind the trailing-edge noise mitigation have been extensively investigated and well understood for serrations at zero flap angle mounted on symmetric airfoils [23–25]. However, its acoustic behavior has been poorly addressed for lifting airfoils retrofitted with serrations at incidence with respect to the incoming flow.

Vathylakis *et al* [26] performed an experimental sensitivity study on airfoil self-noise reduction for different serration flap angles. They retrofitted a NACA 65(12)-10 airfoil with sawtooth serrations mounted at several flap angles, and measured the resulting far-field noise reduction with respect to the straight-edge case. They found that a flap-up position is generally more favorable for broadband trailing-edge noise reduction than a flap-down position.

The mean flow topology, the turbulence statistics and the noise emissions of a NACA 0018 airfoil with sawtooth serrations have been experimentally investigated by Arce-León *et al* [19] for different combinations of flap angles and angles of attack. They found that the degree of serration-flow misalignment significantly affects the level of noise reduction provided by serrations. However, they observed discrepancies between experimental data and a simplified Howe's [12] model (corrected with the maximum local streamline angle deflection) at zero flap angle and angle of attack. Therefore, they concluded that the level of flow-misalignment cannot fully explain the efficiency at which serrations reduce noise.

In a complementary experimental study, Arce-León *et al* [27] further analyzed the effect of the trailing-edge serration-flow misalignment, due to the airfoil incidence and serration flap angle, on the noise levels. They confirmed the previous finding of Gruber *et al* [28] that a serrated airfoil is typically noisier than a baseline airfoil beyond a Strouhal number, based on the boundary-layer thickness and free-stream velocity, approximately equal to 1. Moreover, they proposed a new Strouhal scaling based on the boundary-layer thickness and edge velocity, and noticed that the resulting crossover frequency exhibits a linear modification with changes in the angle of attack, while slightly varying with the free-stream velocity.

Although a few experimental studies have been conducted in the past on the impact of the serration flap angle on the noise reduction effectiveness of serrated trailing-edges, no further insights between the hydrodynamic near-field and noise emissions have been proposed. Therefore, a deeper understanding of the flow physics and noise generation mechanisms associated with serrated trailing-edges at incidence is needed. This situation is relevant for industrial applications where serrations retrofitted to wind turbine or propeller blades might be at incidence with respect to the incoming flow. Hence, the scope of this work is to provide further connections between the hydrodynamic flow features and the resulting far-field noise for a serrated trailing-edge by means of high-fidelity CFD/CAA simulations. For this

purpose, numerical simulations are more suitable than experiments due to their intrinsic capability to extract features of the hydrodynamic near-field without affecting the flow itself and better repeatability.

In this study, a detailed analysis of the unsteady flow properties in proximity of the straight trailing-edge of a free boundary-layer transition lifting NACA 64-618 airfoil is presented first. Then, the impact of the serration flap angle on the mean and the unsteady flows, and its connection with the radiated noise, is addressed. Cases 6 and 7 of the AIAA workshop on Benchmark Problems for Airframe Noise Computations (BANC-V) Category 1 are considered as reference for the straight trailing-edge cases. The numerical results are validated against the measurements made available in the framework of the workshop [29]. The Lattice-Boltzmann Method (LBM) based solver SIMULIA PowerFLOW® is used to obtain the numerical flow solution. The aerodynamic noise generated by the scattering of the hydrodynamic pressure fluctuations at the airfoil trailing-edge is further estimated by using an acoustic analogy based on Farassat's formulation 1A of the Ffowcs-Williams & Hawkings (FW-H) equation applied to the airfoil surface.

The article is organized as follows. In Sec. II, an overview of the lattice-Boltzmann method along with the far-field noise computation approach is presented. The computational setup and test cases are described in Sec. III. The numerical setup validation and the straight trailing-edge analysis are illustrated in Sec. IV. Section V reports the influence of serration flap angle on the hydrodynamic flow field around the add-on device and on its effectiveness in reducing noise. Finally, Sec. VI summarizes the main findings and conclusions of this work.

II. Computational method

A. Lattice-Boltzmann method

The CFD/CAA solver SIMULIA PowerFLOW® is used in this study to obtain the unsteady flow solution. PowerFLOW® solves the Boltzmann equation for the distribution function $g(\mathbf{x}, t, \mathbf{v})$ on a hexahedral mesh automatically generated around solid surfaces. The function g represents the probability to find, in the elementary volume d$\mathbf{x}$ around $\mathbf{x}$ and in the infinitesimal time interval $(t, t + \mathrm{dt})$, a number of fluid particles with velocity in the interval $(\mathbf{v}, \mathbf{v} + \mathrm{d}\mathbf{v})$. The Boltzmann equation is solved by discretizing the space velocity domain into a prescribed number of values in magnitude and direction. These discrete velocity vectors are such that, in a prescribed time step, one particle can be advected from one point of the mesh to N neighboring points, including the point itself. For low-subsonic flow simulations, 19 discrete velocities in three dimensions are used (D3Q19 model). It can be demonstrated that using 19 particle velocity states ensures sufficient lattice symmetry to recover the Navier-Stokes equations for an isentropic (isothermal) flow at low Mach number [30]. The standard LBM formulation is based on the time-explicit advection equation:

$$g_i(\mathbf{x} + \mathbf{v}_i \Delta t, t + \Delta t) - g_i(\mathbf{x}, t) = \Omega_i(\mathbf{x}, t), \tag{1}$$

where g_i represents the particle distribution function along the i-th direction, according to the finite set of discrete velocities $\mathbf{v}_i$, and $\mathbf{v}_i \Delta t$ and Δt are the space and time increments, respectively. The left-hand side of Eq. (1) corresponds to the particle advection, while the right-hand side is the collision operator, which represents the rate of change of g_i resulting from collision (i.e. the interaction of particles). The collision term Ω_i is modeled with the Bhatnagar-Gross-Krook (BGK) approximation [30, 31]:

$$\Omega_i(\mathbf{x}, t) = -\Delta t/\tau [g_i(\mathbf{x}, t) - g_i^{\mathrm{eq}}(\mathbf{x}, t)], \tag{2}$$

where τ is the viscous relaxation time, which is related to the fluid dimensionless kinematic viscosity ν and temperature T according to $\tau = \nu/T + \Delta t/2$, and g_i^{eq} is the equilibrium distribution function, which is related to local hydrodynamic properties [32]. For low Mach numbers, g_i^{eq} is approximated by a second-order expansion with constant temperature [30]:

$$g_i^{\mathrm{eq}} = \rho \xi_i \left[1 + \frac{\mathbf{v}_i \mathbf{u}}{c_s^2} + \frac{(\mathbf{v}_i \mathbf{u})^2}{2c_s^4} + \frac{|\mathbf{u}|^2}{2c_s^2} \right], \tag{3}$$

where ξ_i are the weighting parameters depending on the i-th lattice direction and $c_s = 1/\sqrt{3}$ is the non-dimensional speed of sound in lattice units. Once the distribution function is computed, macroscopic flow density ρ and velocity $\mathbf{u}$ can be determined through discrete integration of g_i:

$$\rho(\mathbf{x}, t) = \sum_i g_i(\mathbf{x}, t), \quad \rho \mathbf{u}(\mathbf{x}, t) = \sum_i g_i(\mathbf{x}, t) \mathbf{v}_i, \tag{4}$$

whereas all the other physical quantities can be obtained from the thermodynamic relationships for an ideal gas.

A wall function approach is used in PowerFLOW® to model boundary-layers on solid surfaces. The wall function model is an extension of the standard law-of-the-wall formulation [33] that includes the effects of favorable and adverse pressure gradients [34]:

$$u^+ = \begin{cases} y^+ & \text{if } y^+ \leq 5 \\ \frac{1}{\kappa} \ln\left(\frac{y^+}{A}\right) + B & \text{otherwise,} \end{cases} \tag{5}$$

where $u^+ = u_s/u_\tau$ and $y^+ = y u_\tau/\nu$ (with $u_\tau = \sqrt{\tau_w/\rho}$ and $\tau_w = \frac{1}{2}\rho C_f u_s^2$ being the friction velocity and the wall shear-stress) are the well-known dimensionless velocity and wall-distance coordinate, respectively. κ and B are empirically determined constants equal to 0.41 and 5 in the logarithmic region ($30 \leq y^+ \leq 300$). In the buffer region ($5 < y^+ < 30$), their values are adjusted to provide continuity between the equations used in the viscous sub-layer and logarithmic regions. The model takes into account the fact that the velocity profile slows down and expands due to an

adverse pressure gradient through the function A. The expression of the scaling function A is given by:

$$A = \begin{cases} 1 + \ell \left| \frac{\mathrm{d}p}{\mathrm{d}\tilde{s}} \right| / \tau_w & \text{if} \quad \hat{\mathbf{u}}_\mathbf{s} \cdot \frac{\mathrm{d}p}{\mathrm{d}\tilde{s}} > 0 \\ 1 & \text{otherwise,} \end{cases} \tag{6}$$

where $\mathrm{d}p/\mathrm{d}\tilde{s}$ is the streamwise pressure gradient, $\hat{\mathbf{u}}_\mathbf{s}$ is the unit vector of the local slip velocity u_s and ℓ is a length-scale of the same order of the unresolved near-wall region. Equation (5) and $\tau_w = \rho u_\tau^2 = \frac{1}{2}\rho C_f u_s^2$ represent a system of two equations in the two unknowns C_f and u_τ, which is solved to specify a wall-shear stress for the wall boundary condition in the LBM scheme consistent with the law-of-the-wall [34]. In this study, simulations are performed by using an Implicit Large Eddy Simulation (ILES) approach, where the inviscid energy cascade through the inertial range is captured by the numerical scheme and the inherent numerical dissipation acts as a sub-grid model [35].

The LBM scheme is solved on a grid composed of cubic volumetric elements (voxels), which are automatically created by the code. Different Variable Resolution (VR) regions can be defined within the fluid domain in order to increase the volume discretization in regions of interest or where high flow gradients are expected. Since a Cartesian mesh is used by the solver, a variable grid resolution by a factor of two is allowed between two adjacent VRs. Moreover, since the solver uses an explicit time-marching scheme based on a unitary Courant-Friedrichs-Lewy condition (i.e. CFL = $|\max(\mathbf{v}_\mathrm{i})\Delta\mathrm{t}|/\Delta\mathrm{x} = 1$), the time step is also varied by a factor of two between two adjacent VRs (and automatically defined by the code according to the voxel size of a certain VR region Δx and the discrete particle velocities $\mathbf{v}_i$). In this way, the solution in coarser VRs is updated at a lower rate compared to finer VRs, and a balanced domain decomposition based on the equivalent number of voxels updated at every time step (i.e. Fine Equivalent Voxel, FEV) allows for an efficient speed-up of the transient flow simulation. The surface of solid bodies is automatically facetized within each voxel intersecting the wall geometry using planar surface elements (surfels). For the no-slip and slip wall boundary conditions at each of these elements, a boundary scheme [36] based on a particle bounce-back process and a specular reflection process is used, respectively.

B. Far-field noise computations

The numerical flow solution provided by the LBM is inherently unsteady and compressible. Moreover, its low dissipation and dispersion properties [37] make it intrinsically suited for aeroacoustic simulations, allowing the extraction of the sound pressure field directly in the near-field. A hybrid CFD/CAA approach is used to compute the far-field noise in order to avoid expensive computations associated to the necessity of accurately resolving the acoustic waves propagation up to the far-field. The Ffowcs-Williams and Hawkings' (FW-H) acoustic analogy is used to compute the far-field noise from the unsteady pressure distribution sampled on the airfoil surface. The FW-H code is part of the post-processing software SIMULIA PowerACOUSTICS®, which is also used for performing statistical and spectral analyses of the

unsteady solution generated by PowerFLOW®. The FW-H solver [38] is based on a forward-time solution [39] of Farassat's formulation 1A [40]. This formulation considers only distributions of acoustic monopoles and dipoles (surface integrals), referred to as thickness and loading terms, and neglects the volume integral (quadrupole term), which accounts for all the possible non-linear effects in the volume surrounding the integration surface (i.e. shock waves, turbulence mixing and propagation effects). However, this formulation is suited for trailing-edge noise prediction, as the boundary-layer pressure fluctuations scattering mechanism, which is related to dipole noise sources ($\sim M^5$), is a more efficient source compared to the quadrupoles in the turbulent wake ($\sim M^8$) at low Mach number [10, 41, 42].

III. Computational setup and test cases

In this study, a NACA 64-618 airfoil with a chord $c = 0.6$ m, a span $s = 0.1c = 0.06$ m and straight trailing-edge is investigated. Cases 6 and 7 from the AIAA BANC-V Workshop Category 1, are considered as experimental benchmark. They correspond to shallow negative and positive angle of attack conditions, respectively. A summary of the flow conditions for each case is reported in Tab. 2. In addition, for each airfoil angle of attack, the airfoil is retrofitted with sawtooth serrations mounted at different flap angles. The serration flap angle β is defined as the angle between the serration and the airfoil chord, positive clockwise. Three serration flap angles are considered, namely: $\beta = 0.0°$ (Serr-chord), $\beta = 6.6°$ (Serr-mid) and $\beta = 13.2°$ (Serr-camber). A sketch of the geometries, as well as of the employed Cartesian coordinate systems, is depicted in Fig. 1. The origin of the airfoil coordinate system (x, y, z) is set at leading-edge midpoint. The x-axis is aligned with the airfoil chord, the y-axis is perpendicular to the former and directed upwards, whereas the z-axis coincides with the airfoil leading-edge with direction defined by the right-hand rule. The local serration coordinate system (x_s, y_s, z_s) has origin on the mid-point at the serration root. The x-axis is aligned with the serration chord, the y-axis is perpendicular to it and the z-axis aligns with the serration span. The sawtooth serration has a thickness $t_s = 0.001$ m, length $h = 0.1c = 0.06$ m and wavelength $\lambda = 0.5h = 0.03$ m, resulting in an aspect ratio of $h/\lambda = 2$. Overall 2 serrations are present along the span.

Table 2 Flow conditions for cases 6 and 7 from AIAA BANC-V Workshop Category 1.

	U_∞ [m/s]	M [-]	Re [-]	T_∞ [K]	ρ_∞ [kg/m^3]	p_∞ [Pa]	α [deg]
Case 6	45.03	0.126	$1.43 \cdot 10^6$	317.6	1.018	92180	−0.88
Case 7	44.98	0.126	$1.43 \cdot 10^6$	317.3	1.019	92180	4.62

The computational domain consists of a box of length equal to $100c$ in both streamwise and wall-normal directions centered around the airfoil trailing-edge. Static pressure and free-stream velocity are prescribed at the outer boundary of the domain, and an acoustic sponge approach is used to damp the out-going acoustic waves, so that backward reflections from the outer boundary are minimized (Fig. 2(a)). Spanwise periodic boundary conditions are applied at the side edges of the computational domain. The free-stream turbulence intensity is set to 0.1%. No transition trips are used

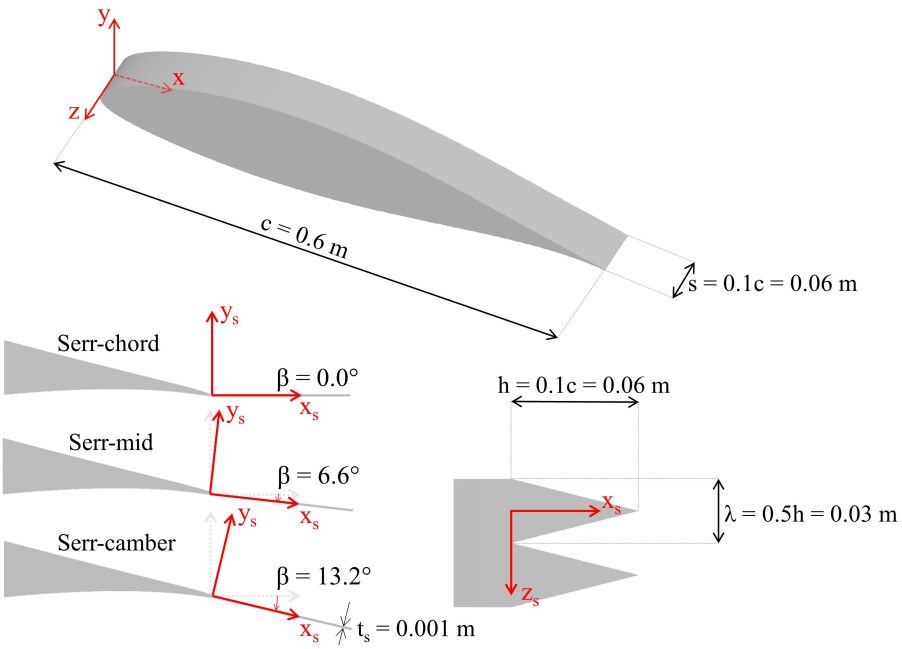

Fig. 1 NACA 64-618 airfoil and serration geometries.

to enforce the laminar-to-turbulent boundary-layer transition. Three different computational grids are investigated, hereinafter referred to as coarse, medium and fine. For each computational grid, the finest VR is set around the expected turbulent boundary-layer regions as defined by XFOIL [43] free-transition computations. The rest of the near-body volume around the airfoil is discretized a level coarser (Fig. 2(b)). A total of 8, 9 and 10 VRs are used to fill the fluid domain for the coarse, medium and fine grids, respectively. For each mesh, Tab. 3 shows the voxel size Δx in the finest VR, the corresponding physical time step (ts), the y^+ in proximity of the trailing-edge, the total number of voxels and the computational cost per flow passage (on Intel Xeon E5-2690 2.90 GHz platform of 360 cores). It is worth recalling that, for $5 \leq y^+ \leq 30$, the coefficients κ and B of the logarithmic law-of-the-wall are adjusted to provide continuity between the viscous sub-layer and logarithmic regions. Hence, for the medium resolution grid, a $y^+ \approx 5.5$ implies that k and B are adapted in such a way that the wall function is still a close approximation of the linear law-of-the-wall, namely $u^+ = \ln(y^+/A)/\kappa + B \approx y^+$. A similar computational setup and near-wall resolution (in terms of y^+) returned a good agreement with experimental results in previous investigations of Avallone *et al* [25] and Ragni *et al* [44], where the LBM had been used to analyze the hydrodynamic flow around combed-sawtooth and slitted serrations. Throughout this paper, the noise radiation is computed by using a FW-H analogy applied to a surface mesh fitted to the airfoil surface wall. The flow is sampled after 10 initial flow passages (0.13 sec of physical time) that constitute the transient phase of the simulation. The unsteady pressure on the airfoil surface is sampled at 84 kHz for a total of 8 flow passes (0.10 sec). Fourier transformed data is obtained with 50% overlap and Hamming windowing to further smooth the spectra.

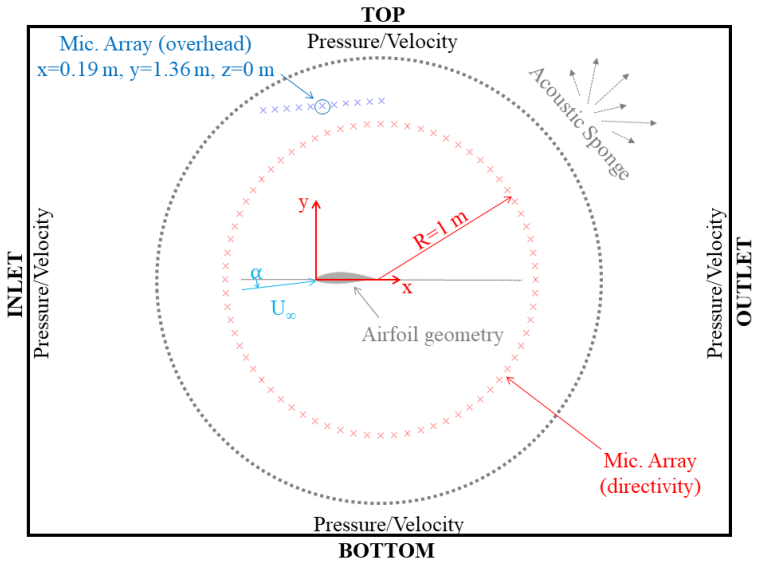

(a) *Computational setup (boundaries and sponge not to scale)*

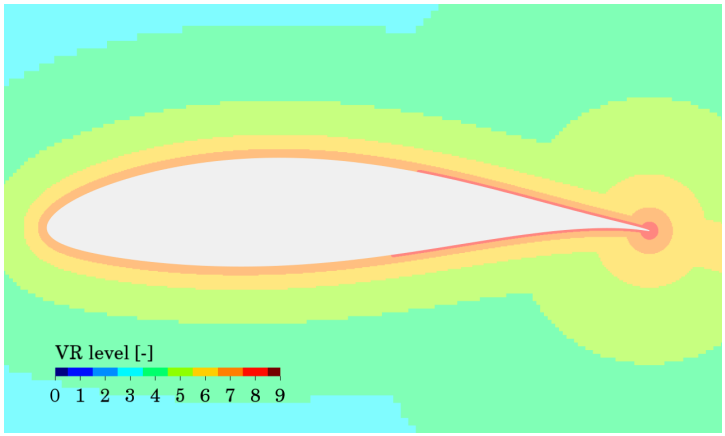

(b) *Near-body mesh (medium resolution)*

Fig. 2 Sketch of the computational setup and grid.

Table 3 Mesh resolution, grid size and computational cost.

Resolution	# VR	Δx [mm]	y^+ [-]	ts [s]	# Voxels	# FEVs	CPUh/flow passage
Coarse	8	0.234	10.8	$3.71 \cdot 10^{-7}$	$48.3 \cdot 10^6$	$23.0 \cdot 10^6$	350
Medium	9	0.117	5.5	$1.86 \cdot 10^{-7}$	$14.2 \cdot 10^7$	$80.7 \cdot 10^6$	2100
Fine	10	0.059	2.6	$9.28 \cdot 10^{-8}$	$50.8 \cdot 10^7$	$30.1 \cdot 10^7$	15600

IV. Straight trailing-edge: analysis and setup validation

In this section, numerical results for the straight trailing-edge airfoil are discussed and compared to the experimental data from the AIAA BANC-V Workshop Category 1 (cases 6 and 7). The quality of the numerical results is assessed in terms of surface pressure distribution, boundary-layer characteristics, wall-pressure spectrum, far-field noise and

spanwise coherence length. In addition, a mesh resolution study is performed on both aerodynamic and aeroacoustic quantities in order to verify the grid independence of the numerical results.

A. Pressure distribution and trailing-edge boundary-layer profiles

Figure 3 shows the mean pressure distribution against the experimental measurements. For both cases 6 and 7, the numerical results are in a very good agreement with the experimental data, except for $x/c \approx 0.6$ (case 6) and $x/c \approx 0.5$ (case 7), where the numerical results do not show the presence of the laminar-separation bubble occurring in the experiments. Preliminary simulations with turbulent intensity equal to 0.05%, comparable to that measured during the experiments [29], have also been attempted by the authors without showing any significant impact on the pressure-coefficient distribution and boundary-layer transition. Therefore, it is believed that the discrepancies observed on the pressure-coefficient distributions are primarily ascribable to artifacts of the numerical method. Overall, the pressure coefficient does not appear to be particularly sensitive to the three different grid resolutions considered, as expected due to the relatively low y^+ values. Only a minor difference between the coarse mesh and the finer ones around $x/c = 0.6$ on the suction side of the airfoil is observed. This result suggests that the coarse mesh could be used for purely aerodynamic calculations.

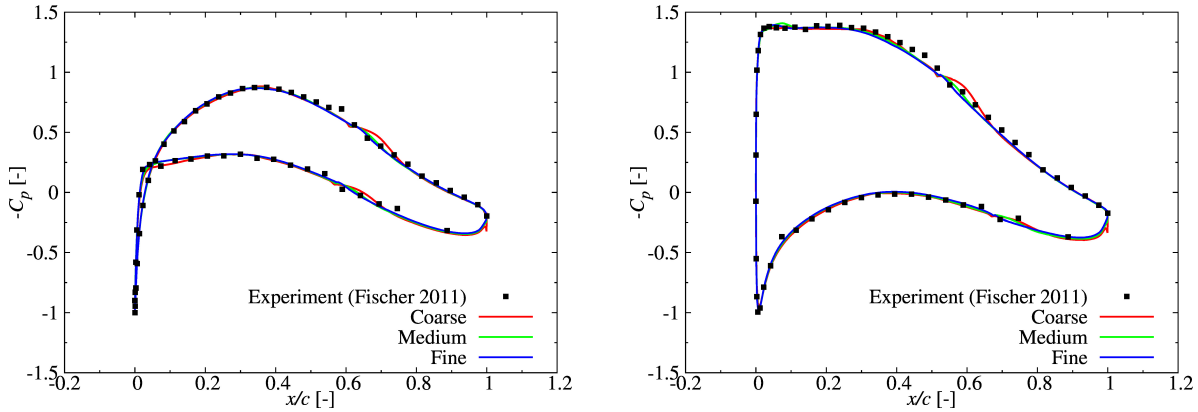

(a) *Case 6 ($\alpha = -0.88°$)* (b) *Case 7 ($\alpha = 4.62°$)*

Fig. 3 Time-average pressure coefficient distribution over the airfoil surface. Experimental results from Fischer [29].

The time-averaged streamwise velocity profiles $\langle u \rangle$ at $x/c = 0.975$ on the suction side are shown in Fig. 4. A satisfactory agreement is found between numerical results and hot-wire anemometer measurements for each case and resolution level, especially for $\alpha = -0.88°$ (case 6) and the inner part of the boundary-layer. Overall, the predicted boundary-layer edge velocity results to be relatively higher than the one measured for cases 6 and 7. The medium and fine resolution levels show a satisfactory convergence trend, while a much thicker boundary-layer is observed in the coarse grid.

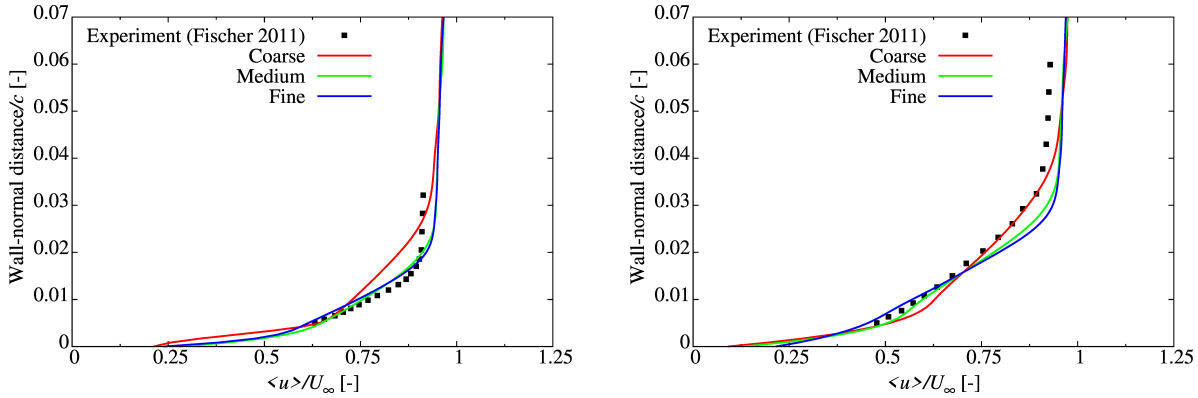

(a) *Case 6* ($\alpha = -0.88°$) (b) *Case 7* ($\alpha = 4.62°$)

Fig. 4 Mean streamwise velocity profile at $x/c = 0.975$ on the suction side. Experimental results from Fischer [29].

The time-averaged Reynolds stress profiles $\langle u'u' \rangle$, $\langle v'v' \rangle$ and $\langle u'v' \rangle$ at $x/c = 0.975$ on the suction side are depicted in Fig. 5. u' and v' represent the streamwise and wall-normal velocity fluctuation components, respectively. For both cases 6 and 7, the streamwise fluctuations $\langle u'u' \rangle$ are predicted with a satisfactory level of accuracy, with the numerical profiles correctly approaching the non-dimensional value of 0 outside the boundary-layer. Experimental data not fully converging to zero might be a result of the hot-wire calibration and averaging. A similar behavior can be also noticed for the wall-normal $\langle v'v' \rangle$ and shear $\langle u'v' \rangle$ components that deviate away from the experimental data close to the wall. Such differences could be attributed to the use of hot-wire anemometers, which might have resulted in erroneous velocity data due to the additional heat losses in proximity of the wall [45], as well as to the slightly delayed prediction of the boundary-layer transition process (as it will be shown in Sec. IV.B). Overall, a good level of grid convergence is observed between the medium and fine computational meshes, with only variations in the the prediction of the maximum values of the boundary-layer velocity fluctuation profiles, especially for $\alpha = 4.62°$ (case 7).

B. Laminar-to-turbulent boundary-layer transition

As introduced in Sec. III, the free transition cases 6 and 7 of the AIAA BANC-V Workshop Category 1 are simulated in this study without enforcing the development of the turbulent boundary-layer by means of transition trips. In order to quantitatively assess the laminar-to-turbulent boundary-layer transition process, Tab. 4 shows the comparison between the measured transition locations and the numerical ones. Since the transition on the pressure side was not measured during the experimental campaign [29], the predictions from viscous XFOIL [43] simulations are also reported. In Tab. 4, the experimental and XFOIL results represent the effective transition points (i.e. the position where the boundary-layer is fully turbulent), whereas the numerical ones are provided in terms of initial and final locations of the transition process, which are based on the minimum and maximum chordwise values of the surface skin friction coefficient, respectively. For the suction side, the chordwise position where the boundary-layer is fully turbulent is

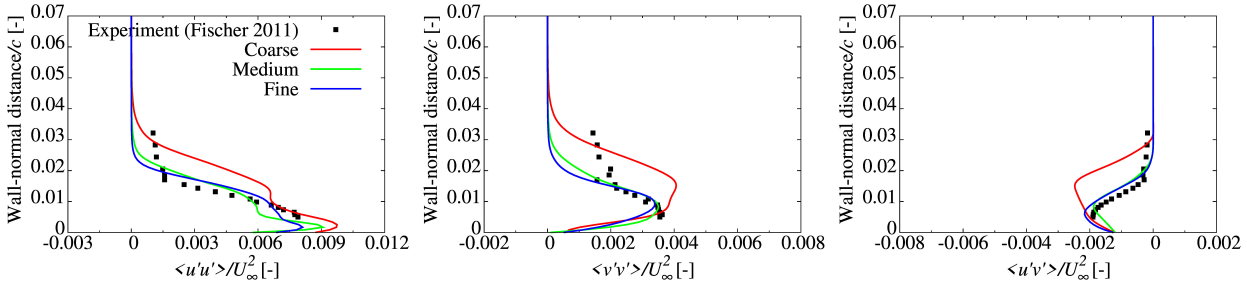

(a) *Case 6* ($\alpha = -0.88°$)

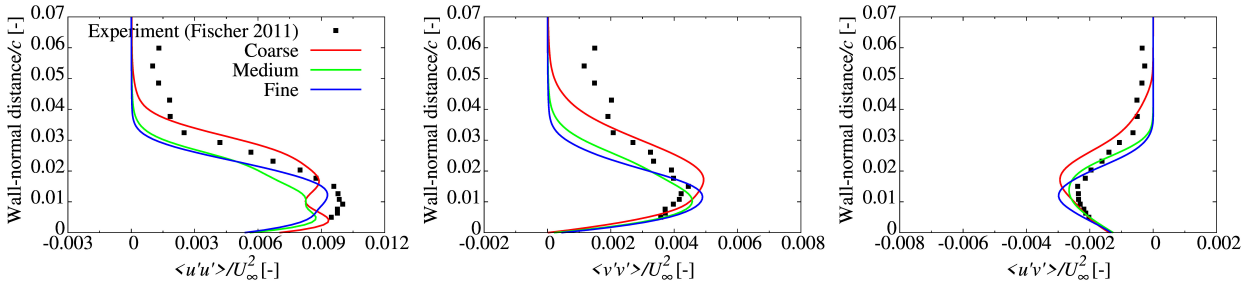

(b) *Case 7* ($\alpha = 4.62°$)

Fig. 5 Time-averaged Reynolds stress profiles at $x/c = 0.975$ on the suction side. Experimental results from Fischer [29].

delayed from 15%, for the coarse grid and both angles of attack, to 8% ($\alpha = -0.88°$) and 5% ($\alpha = 4.62°$) for the finer mesh. Regarding the pressure side, no experimental data is available, but the same level of transition delay is expected by comparing numerical and XFOIL results, and considering how the latter correlates with the experiments on the suction side. However, a good convergence trend can be noted between the medium and fine meshes, for which the boundary-layer transition process takes place within roughly the same chordwise extension. The slightly delayed prediction of the end of the laminar-to-turbulent transition might be another cause for the slight over-prediction of the wall-normal $\langle v'v' \rangle$ and shear $\langle u'v' \rangle$ Reynolds stress peak values observed in Fig. 5.

Table 4 Laminar-to-turbulent boundary-layer transition location in percentage of chord (x/c). Experimental results from Fischer [29].

Case 6	Experiment (Fischer 2011)	XFOIL	Coarse	Medium	Fine
Suction side	0.65	0.62	0.62 ÷ 0.80	0.63 ÷ 0.75	0.62 ÷ 0.73
Pressure side	–	0.58	0.60 ÷ 0.82	0.58 ÷ 0.70	0.58 ÷ 0.68
Case 7	Experiment (Fischer 2011)	XFOIL	Coarse	Medium	Fine
Suction side	0.56	0.52	0.56 ÷ 0.71	0.54 ÷ 0.64	0.52 ÷ 0.61
Pressure side	–	0.69	0.74 ÷ 0.90	0.69 ÷ 0.79	0.67 ÷ 0.74

C. Wall-pressure fluctuation spectrum

Figure 6 shows the comparison between the numerical and experimental wall-pressure power spectral densities Φ_{pp} at $x/c = 97.5\%$ and $x/c = 95\%$ on the suction and pressure sides. In Fig. 6, Φ_{pp} is plotted as a function of the non-dimensional frequency expressed in terms of Strouhal number $St_c = fc/U_\infty$, based on the airfoil chord c and free-stream velocity U_∞. A good convergence trend is found between the medium and fine computational grids in the frequency of interest for turbulent boundary-layer trailing-edge noise ($4 < St_c < 100$) [7], with only small differences observed at low frequency on the pressure side (Figs. 6(c) and 6(d)), whereas the coarse mesh presents larger pressure fluctuations at low and mid frequencies. As expected, the numerical wall-pressure spectra show higher fluctuations as the resolution increases at very high frequencies ($St_c > 100$), due to capability of the computational mesh to capture smaller scales of turbulence. For each angle of attack, the numerical setup is able to reproduce the general shape and trend of the experimental wall-pressure fluctuation spectra, as well as the fact that the suction side (Figs. 6(a) and 6(b)) is more energetic than the pressure one (Figs. 6(c) and 6(d)). A power decay $\propto f^{-1}$ typical of a fully developed turbulent boundary-layer is found at mid-to-high frequencies, while at very high frequency the spectra show a slope $\propto f^{-5}$ as a consequence of the viscous dissipation [46]. Besides this, a large over-prediction up to 10 dB/Hz is observed in the numerical predictions compared to the measurements.

To better clarify this aspect, the wall-pressure spectra computed with three different semi-empirical models are also compared to the numerical and experimental results in Fig. 6. The semi-empirical models are Schlinker & Amiet's [1], Rozenberg's [47] and Kamruzzaman's [48], which are fed with boundary-layer parameters extracted from the numerical simulations (reported in Tab. 5). As expected, the three different semi-empirical models show a certain sensitivity to the input data. The semi-empirical results compare more favorably with numerical predictions than experiments, except for the Schlinker-Amiet's model on the suction side for both $\alpha = -0.88°$ and $\alpha = 4.62°$. This might be caused by the fact that the Schlinker-Amiet's model does not account for adverse pressure gradient effects, which are known to increase the amplitude of the wall-pressure spectrum [47, 48]. On the one hand, these results suggest that the experimental wall-pressure spectra might be affected by some measurement errors. On the other hand, having performed a wall-modeled implicit large eddy simulation (ILES) does not guarantee that the numerical wall-pressure spectra correspond to those extracted from a fully resolved direct numerical simulation (DNS). A companion far-field noise analysis by means of Roger & Moreau's [5] semi-analytic trailing-edge model, fed with the experimental wall-pressure spectra, is performed in the next subsection for further clarification of such discrepancies.

D. Far-field noise

In Fig. 7, far-field noise computations carried out using the FW-H acoustic analogy applied to the airfoil surface are validated against the experimental beam-forming data. The far-field noise is obtained by approximating the experimental beam-forming array [29] using a line of 11 streamwise microphones centered on the experimental array center ($x = 0.19$

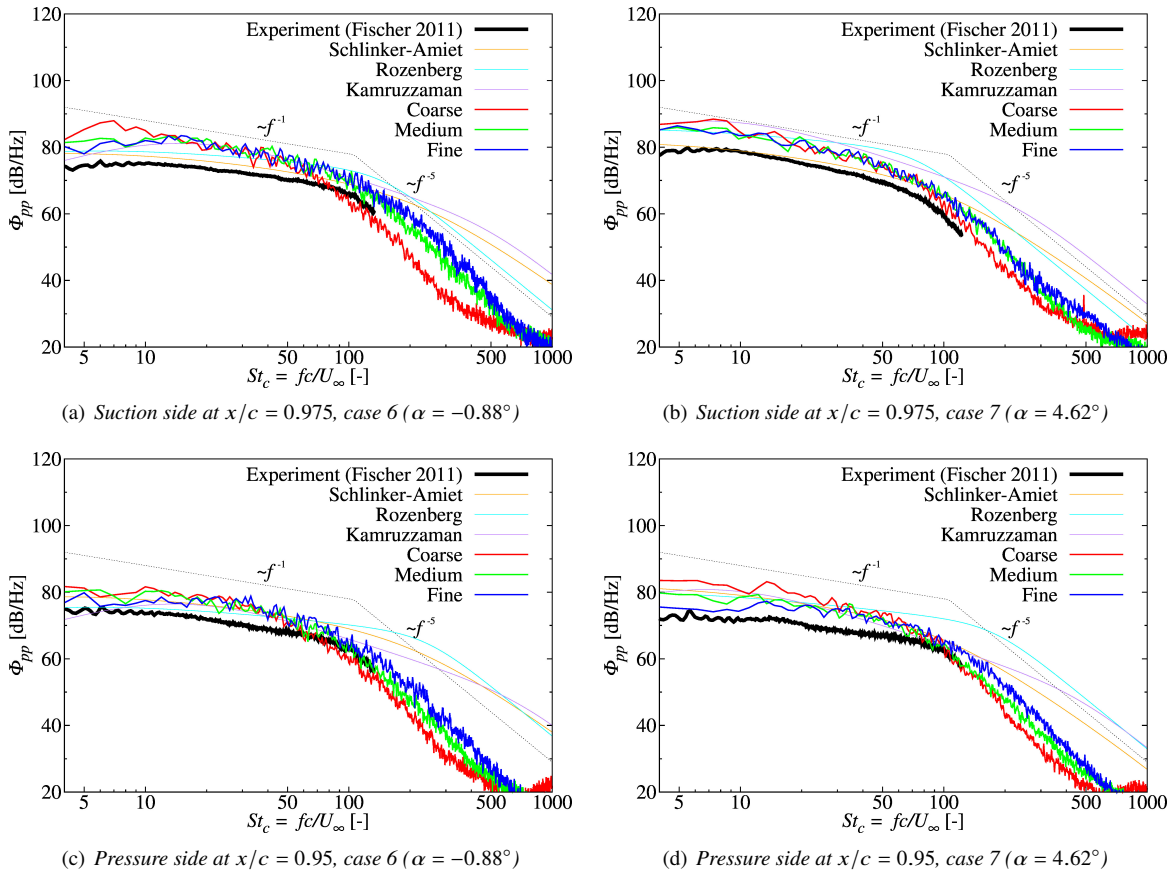

(a) *Suction side at* $x/c = 0.975$*, case 6* ($\alpha = -0.88°$)

(b) *Suction side at* $x/c = 0.975$*, case 7* ($\alpha = 4.62°$)

(c) *Pressure side at* $x/c = 0.95$*, case 6* ($\alpha = -0.88°$)

(d) *Pressure side at* $x/c = 0.95$*, case 7* ($\alpha = 4.62°$)

Fig. 6 Power spectral density of the wall-pressure Φ_{pp} in proximity of the trailing-edge. Experimental results from Fischer [29]. Semi-empirical results from Schlinker & Amiet's [1], Rozenberg [47] and Kamruzzaman's models [48].

m, $y = 1.62$ m, $z = 0$ m) and averaging over them. This overhead numerical microphone array is depicted in blue in Fig. 2(a). The far-field sound pressure level in 1/3-octave band is normalized for a reference observer distance $R_r = 1$ m and span length $s_r = 1$ m in order to allow for comparison with the experiments, where a span of 0.6 m resulting from the beam-forming integration region is used. The following formula is used for scaling [46]:

$$\Phi_{aa} = \Phi_{aa}^{\text{raw}} + 20\log_{10}(R/R_r) - 10\log_{10}(s/s_r) \tag{7}$$

where Φ_{aa} represents the normalized sound pressure level and Φ_{aa}^{raw} is the raw computed or measured sound pressure level for a generic observer radius R and span s. To shed more light on the discrepancies observed between the numerical and measured wall-pressure spectra (Fig. 6), the far-field noise predictions computed with Roger & Moreau's semi-analytical trailing-edge noise model [5], fed with the experimental wall-pressure spectra at the trailing-edge, are also shown in Fig. 7. In addition to the wall-pressure spectra at the trailing-edge, Roger & Moreau's model also requires the spanwise coherence length l_z as input. In this study, the spanwise coherence length supplied to the analytical

Table 5 Boundary-layer parameters extracted from the numerical simulations (medium resolution) used in semi-empirical wall-pressure spectrum model [1, 47, 48] and semi-analytical trailing-edge noise model [5].

Suction side at $x/c = 0.975$			Case 6	Case 7
Edge velocity	U_e	[m/s]	42.62	43.41
Boundary-layer thickness	δ	[m]	0.0147	0.0273
Displacement thickness	δ^*	[m]	0.0027	0.0055
Momentum thickness	Θ	[m]	0.0017	0.0031
Wall shear stress	τ_w	[N/m^2]	2.704	1.60
Pressure gradient	$\mathrm{d}p/\mathrm{d}x$	[Pa/m]	4786.6	4250.0
Pressure side at $x/c = 0.95$			Case 6	Case 7
Edge velocity	U_e	[m/s]	43.20	43.76
Boundary-layer thickness	δ	[m]	0.0292	0.0394
Displacement thickness	δ^*	[m]	0.0029	0.0058
Momentum thickness	Θ	[m]	0.0019	0.0034
Wall shear stress	τ_w	[N/m^2]	2.542	2.98
Pressure gradient	$\mathrm{d}p/\mathrm{d}x$	[Pa/m]	-172.50	263.7

trailing-edge model is estimated with the Corcos' model [49], namely:

$$l_z(f) = \frac{b_c u_c}{2\pi f}, \tag{8}$$

where b_c is a constant, typically chosen between 1.2 and 1.7 [50], while u_c is the convection velocity. u_c is computed as $u_c = \zeta U_e$, where U_e is the edge velocity and ζ a parameter usually taken between 0.6 and 0.8. To account for the influence of such parameters on the far-field noise predicted by Roger & Moreau's trailing-edge noise model, which is proportional to b_c and ζ through the Corcos's model, the semi-analytical results are computed for $(b_c = 1.2, \zeta = 0.6)$ and $(b_c = 1.7, \zeta = 0.8)$. This allows to identify the range between the lowest and highest far-field noise levels predictable by Roger & Moreau's model fed with the available experimental wall-pressure spectra.

For case 6 (Fig. 7(a)), a good agreement is found between numerical and experimental results, with only 1-2 dB over-estimation for the medium and fine grids. Regarding case 7 (Fig. 7(b)), the FW-H prediction fits the experimental data up to $St_c = 20$, whereas for higher frequencies a certain over-prediction can be observed. It is worth mentioning that a similar over-prediction at high frequency was also found by Lee *et al* [51] by using Howe's trailing-edge model [52] fed with empirical wall-pressure spectra [53] for the same benchmark case. Overall, a good convergence trend is observed between the medium and fine cases for both the angles of attack, with only a minor scatter of the numerical predictions within 1 dB throughout the frequencies of interest. Regarding the results from Roger & Moreau's trailing-edge model fed with experimental wall-pressure spectra, a certain under-estimation of the far-field noise levels is observed for $(b_c = 1.2, \zeta = 0.6)$, while a good agreement with experiments is found for $(b_c = 1.7, \zeta = 0.8)$, especially for case 6.

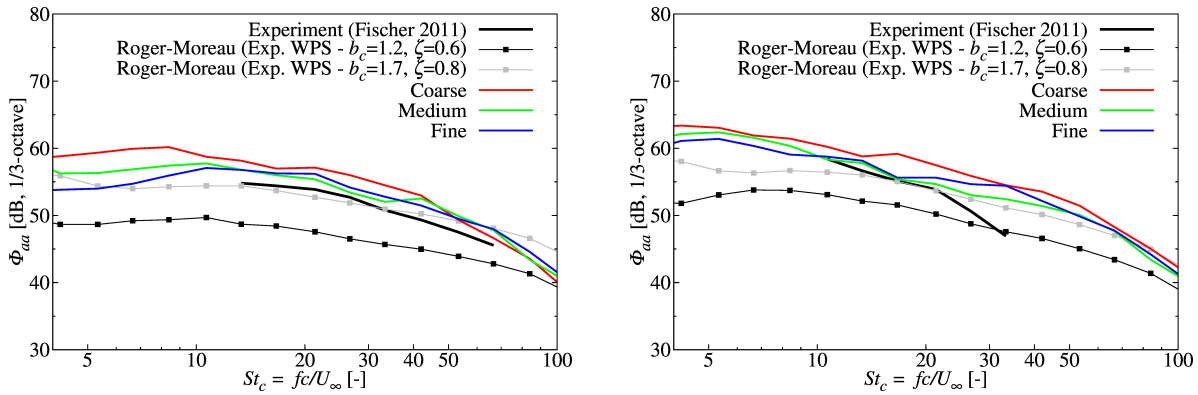

(a) *Case 6* ($\alpha = -0.88°$) (b) *Case 7* ($\alpha = 4.62°$)

Fig. 7 Far-field sound pressure level in 1/3-octave band Φ_{aa} at ($x = 0.19$ m, $y = 1.62$ m, $z = 0$ m). Experimental results from Fischer [29]. Roger & Moreau's trailing-edge model [5] fed with the experimental wall-pressure spectra.

Interestingly, both numerical and semi-analytical predictions show similar sound pressure level slopes, which differ from the experimental one in the range $20 < St_c < 30$, for case 7. The fact that the numerical far-field noise is overall higher than the measured one might be a consequence of the over-prediction of the numerical wall-pressure spectra in proximity of the trailing-edge (Fig. 6). On the other hand, the semi-analytical predictions falling on average below the experimental far-field noise results might be associated to the relatively low experimental wall-pressure spectra shown in Fig. 6. In view of the above, the discrepancies observed in the wall-pressure spectra and far-field noise results could be ascribable to a combination of factors in both simulations and experiments. Future studies based on wall-resolved LES or DNS computations, as well as independent measurements for similar flow configurations, might help resolve the origin of the aforementioned differences.

E. Wall-pressure fluctuations spanwise coherence and coherence length

The straight-edge analysis and validation are concluded by focusing on the spanwise turbulent flow statistics, which is known to play a relevant role for trailing-edge noise, as the scattering process is related to the properties of the vortical field in proximity of the trailing-edge [5]. In this sense, an important parameter to track is the spanwise coherence length l_z, as the far-field noise spectrum is proportional to l_z according to Howe's trailing-edge noise theory [52]. This parameter can be conceived as the length of a source term scattering at the trailing-edge and is a function of the frequency f:

$$l_z(f) = \lim_{L\to\infty} \int_0^L \sqrt{\gamma^2(f,\eta)}\mathrm{d}\eta, \tag{9}$$

where $\gamma^2(f,\eta)$ is the squared coherence function of the wall-pressure signals between two points spaced by η along the spanwise direction z. The squared coherence function γ^2 is in turn defined as the squared magnitude of the cross-spectrum $\mathrm{C}(f, z_1, z_2)$ of the two signals, sampled at two points z_1 and $z_2 = z_1 + \eta$ along the spanwise coordinate

z, divided by the auto-spectrum of both signals at each frequency, namely:

$$\gamma^2(f,\eta) = \frac{|\mathrm{C(f,z_1,z_2)}|^2}{|\mathrm{C(f,z_1,z_1)}||\mathrm{C(f,z_2,z_2)}|}. \tag{10}$$

In order to compare the numerical coherence length to the experimental one, the squared coherence function has to be evaluated first. Figure 8 depicts the spanwise squared coherence contours at $x/c = 0.975$ on the suction side.

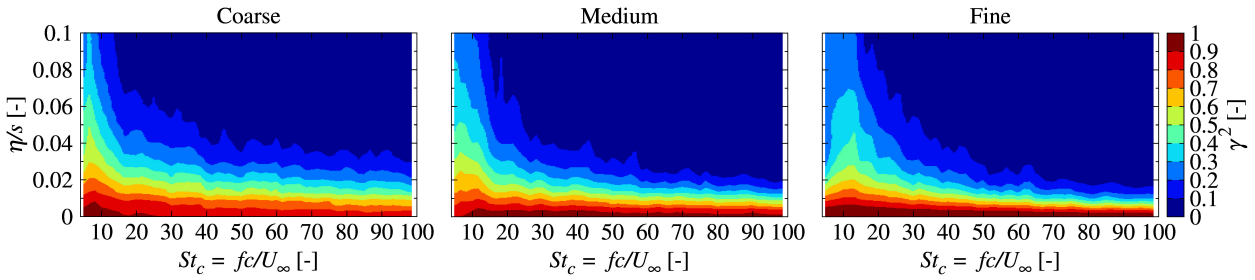

(a) *Case 6 ($\alpha = -0.88°$)*

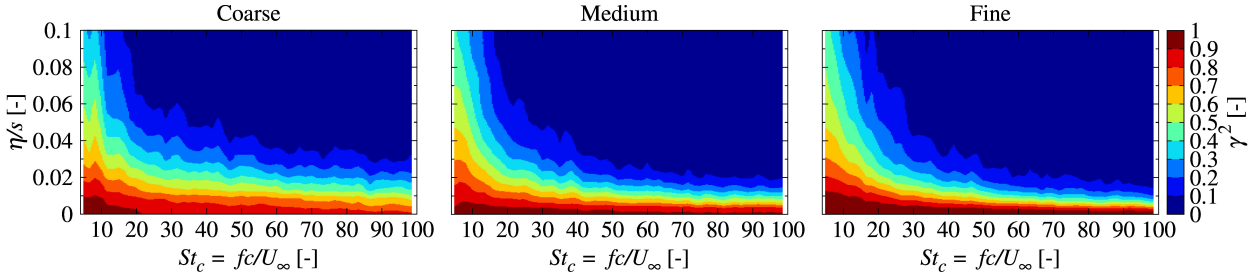

(b) *Case 7 ($\alpha = 4.62°$)*

Fig. 8 Magnitude of the spanwise squared coherence function γ^2 at $x/c = 0.975$ on suction side. Spanwise separation distance η normalized by the simulated airfoil span s.

For both cases 6 and 7, a peak around $St_c = 10$ is observed, after which γ^2 decays as the frequency increases, as expected for turbulent flows. In addition, the spanwise squared coherence drops down to relatively low values for separation distances within 10% of the airfoil span. This implies that the simulated span is large enough to include source regions that radiate noise independently from the neighboring ones in a statistical sense [54]. For a given frequency, a more rapid decay of γ^2 is observed as the resolution increases. This suggests that a refinement of the computational mesh, especially from the coarse grid to medium one, leads to a prediction of less coherent turbulent structures for larger spanwise separation distances. Overall, a good convergence trend is observed between medium and fine resolutions, especially in the mid to high frequency range.

In Fig. 9 the comparison between the experimental coherence length l_z at $x/c = 0.975$ on the suction side and the numerical ones is shown. It should be pointed out that the numerical coherence length is not rigorously computed by using Eq. (9), as the squared coherence function does not approach zero for large separation distances η, thus leading to convergence issues of the direct integration of γ [55]. To overcome this issue, the spanwise coherence length l_z is

evaluated by means of a curve fitting approach based on an exponential function [56, 57] and performed on the spanwise coherence $\gamma(f,\eta)$ for each discrete frequency, namely:

$$\gamma(f,\eta) = \mathrm{e}^{-|\eta|/l_z(f)}. \tag{11}$$

Note that, for each discrete frequency, the exponential fitting is performed by neglecting those separation distances for which the coherence function γ does not show a convergent trend towards 0, as depicted in Fig. 10 for four different values of the non-dimensional frequency (St_c = 8, 12, 36 and 72). For case 6 (Fig. 9(a)), the agreement between the measured and numerical spanwise coherence length is satisfactory for all the frequencies. The only discrepancy is observed around St_c = 6, where the sharp peak of the measured coherence length is not reproduced in the numerical ones. This might be a consequence of the larger bandwidth used in the numerical results. For case 7 (Fig. 9(b)), the numerical results also match the experiments in a quite satisfactory way, although a slight over-prediction is found below St_c = 6. Again, the medium and fine resolution meshes show a quite good convergence trend.

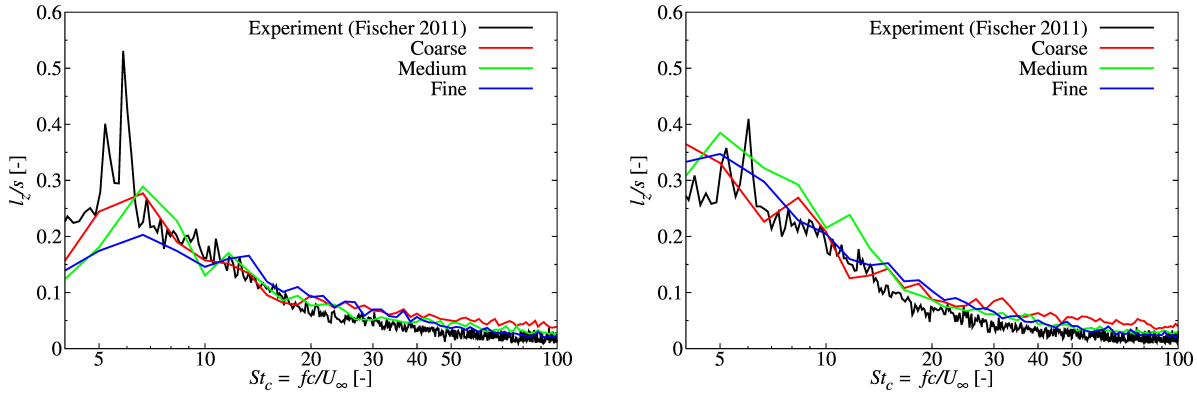

(a) *Case 6* ($\alpha = -0.88°$) (b) *Case 7* ($\alpha = 4.62°$)

Fig. 9 Spanwise coherence length l_z normalized by the simulated airfoil span s at x/c = 0.975 on the suction side. Experimental results from Fischer [29].

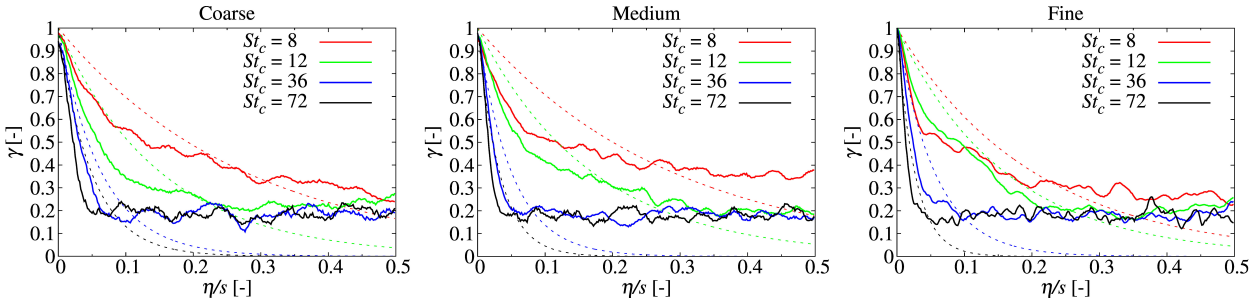

(a) *Case 6* ($\alpha = -0.88°$)

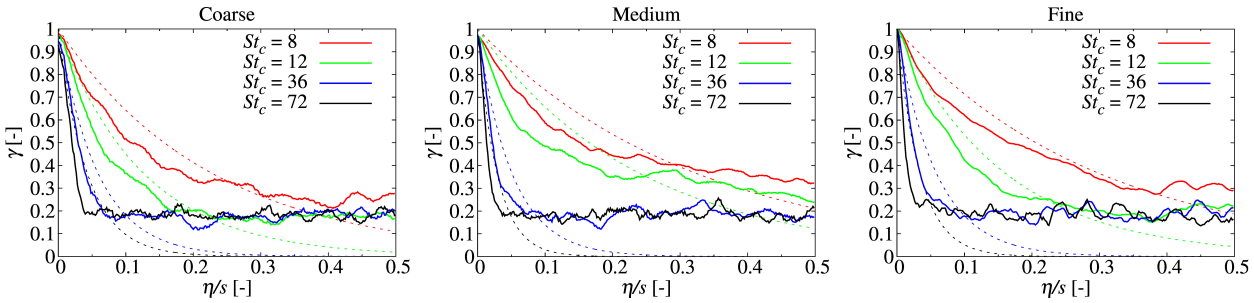

(b) *Case 7* ($\alpha = 4.62°$)

Fig. 10 Magnitude of the spanwise coherence function γ at $x/c = 0.975$ on suction side for different normalized frequencies St_c: comparison between raw data (solid line) and exponential fit (dashed line).

Overall, the medium resolution setup provided quite similar flow statistics in proximity of the trailing-edge and noise predictions compared to the fine one, with a computational time almost one order of magnitude lower (Tab. 3). Therefore, in order to keep the computational cost relatively low without sensibly affecting the numerical results, the medium resolution grid is used in what follows to investigate the effect of the serration flap angle on the hydrodynamic near-field and acoustic far-field.

V. Serrated trailing-edge: analysis of flap angle effects

In this section, the effect of the flap angle upon the aerodynamic and acoustic behavior of the serrated edge is numerically investigated. For each airfoil angle of attack, the NACA 64-618 profile is retrofitted with sawtooth serrations mounted at three different flap angles: $\beta = 0.0°$, $\beta = 6.6°$ and $\beta = 13.2°$. The former correspond to a condition such that the serration is aligned with the airfoil chord (Serr-chord), whereas the latter with the local tangent to the suction side at $x/c = 0.99$ (Serr-camber). The $\beta = 6.6°$ case represents an intermediate condition to the previous ones (Serr-mid). No experimental data is available for such serrated cases. Therefore, only numerical results are shown, obtained using the computational setup validated in Sec. IV. Although not shown for the sake of conciseness, it is verified that for the cases under examination the presence of the serrations and their flap angle do not significantly affect the natural boundary-layer transition process, the wall-pressure fluctuations spectrum, integral boundary-layer parameters and

spanwise pressure coherence length upstream the trailing-edge. Finally, it should be recalled that the typical coherence length at the frequencies of interest for the present study (where significant noise reduction due the serration can occur, i.e. $4 < St_c < 32$ as it will be shown in Sec. V.B) must be substantially smaller than the spanwise extent of the computational domain for the results to be reliable. This requirement is satisfied by the employed computational setup, as observed in Fig. 9, which shows that for both cases the coherence length in the range $4 < St_c < 32$ is considerably lower than the simulated airfoil span extension.

A. Pressure distribution

Figure 11 shows the influence of the serration flap angle on the time-average pressure coefficient distribution over the airfoil surface for $\alpha = -0.88°$ and $\alpha = 4.62°$. The pressure coefficient distributions are extracted on a longitudinal plane passing through the serration tip. Although not shown for the sake of brevity, it is observed that the time-average pressure distribution is independent from the spanwise position of the plane of extraction for $0 \leq x/c \leq 1$. Table 6 show the impact of the flap angle on the sectional lift and drag coefficients for both $\alpha = -0.88°$ and $\alpha = 4.62°$.

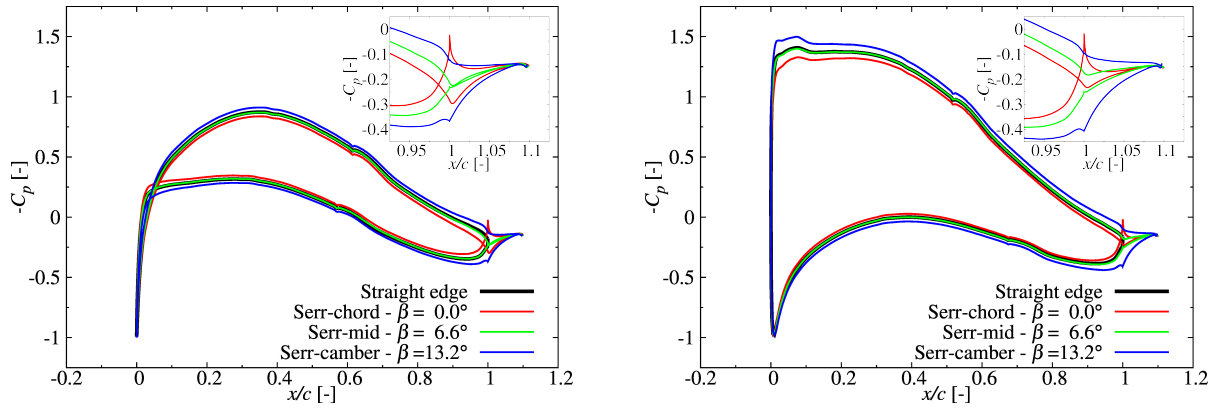

(a) *Case 6 ($\alpha = -0.88°$)* (b) *Case 7 ($\alpha = 4.62°$)*

Fig. 11 Time-average pressure coefficient distribution over the airfoil and serration surfaces.

For both angles of attack, the serration being at incidence with respect to the upcoming flow results in a change of circulation and, in turn, of the loading of the airfoil. On the one hand, the chord-aligned serration ($\beta = 0.0°$) induces a reduction of the lift generated by the airfoil compared to the straight edge configuration, as well as a favorable pressure gradient going from the suction to the pressure side of the serration. On the other hand, the camber-aligned serration ($\beta = 13.2°$) yields to an increment of the airfoil lift with respect to the non-serrated case and to the generation of an adverse pressure gradient between the suction and pressure sides of the add-on. A more neutral behavior is exhibited by the intermediate serration case ($\beta = 6.6°$) for which, being the add-on more aligned with the mean-flow streamlines leaving the airfoil trailing-edge (as it will be shown in Sec. V.E), there is no evident variation of the airfoil lift and only a weak adverse pressure gradient is generated across the serration tooth, moving from the suction to the pressure side.

Table 6 Effect of serration flap angle on sectional lift and drag coefficients.

Case 6 ($\alpha = -0.88°$)	C_L [-]	C_D [-]
Straight edge	0.419	0.007
Serr-chord - $\beta = 0.0°$	0.328	0.006
Serr-mid - $\beta = 6.6°$	0.411	0.007
Serr-camber - $\beta = 13.2°$	0.508	0.008
Case 7 ($\alpha = 4.62°$)	C_L [-]	C_D [-]
Straight edge	1.060	0.009
Serr-chord - $\beta = 0.0°$	0.982	0.010
Serr-mid - $\beta = 6.6°$	1.066	0.011
Serr-camber - $\beta = 13.2°$	1.179	0.012

Serration flap angles that increase the overall blade loading might impose additional challenges from a structural viewpoint and require the addition of additional mass and stiffness to the retrofitted blade, especially for wind turbine blades. In terms of noise radiation, the change in the steady air-loads can affect both the steady loading noise and turbulent boundary-layer trailing-edge noise generation. First, a serrated blade generating more/less lift would eventually produce more/less steady loading noise at blade-passing frequencies falling in the frequency range where turbulent boundary-layer trailing-edge noise reduction due to serrations may occur. Second, a more loaded blade might cause an earlier laminar-to-turbulent boundary-layer transition and yield to higher turbulent pressure fluctuations approaching the serrated trailing-edge. This can have an impact on the turbulent boundary-layer trailing-edge noise generation, in addition to that associate to the local changes of the hydrodynamic field induced by a certain serration flap angle. In view of this, the potential benefits on trailing-edge noise reduction given by a specific serration flap angle, should be evaluated in conjunction with its impact on rotor performances, aerodynamic loading, steady tonal noise and boundary-layer transition. As mentioned earlier, for the configurations examined in this study, the serrations and their flap angle do not significantly influence the boundary-layer transition process and the pressure statistics of the flow approaching the serrated trailing-edge. Therefore, it is expected that the turbulent boundary-layer trailing-edge noise variations with respect to the straight edge (Secs. V.B and V.C) are primarily due to local flow changes induced by the serration itself.

B. Far-field noise reduction

The effect of the serration flap angle on the far-field trailing-edge noise reduction with respect to the straight trailing-edge is analyzed in this subsection. For the three different flap angles, Fig. 12 depict the 1/3-octave band sound pressure level reduction with respect to the straight trailing-edge, $\Delta\Phi_{aa} = \Phi_{aa}^{\mathrm{str}} - \Phi_{aa}^{\mathrm{serr}}$ (where Φ_{aa}^{str} and $\Phi_{aa}^{\mathrm{serr}}$ are the far-field noise spectra of the straight and serrated edge, respectively), at the center of the overhead microphone array ($x = 0.19$ m, $y = 1.62$ m, $z = 0$ m) for $\alpha = -0.88°$ and $\alpha = 4.62°$. The normalized frequency range examined here is $4 < St_c < 32$, which corresponds to a dimensional frequency ranging from 300 Hz to 2400 Hz. As expected, for each case the noise

reduction varies with the frequency, but different trends are observed between the three different flap angles. The intermediate serration flap angle ($\beta = 6.6°$) shows the best noise suppression behavior among the three examined serration configurations, except for $\alpha = -0.88°$ and $St_c < 7$. For this configuration, a noise reduction is observed throughout the frequency range of interest, with a maximum noise attenuation of 4 dB at low and mid frequencies, for $\alpha = -0.88°$ (Figure 12(a)), and 6 dB at $St_c \approx 6$, for $\alpha = 4.62°$ (Figure 12(b)). On the contrary, the serrations aligned with the airfoil chord and camber do not exhibit consistent trends as the airfoil angle of attack varies. Specifically, for $\alpha = -0.88°$ the camber-aligned serration outperforms the chord-aligned one by providing a noise reduction up to $St_c \approx 13$, after which an increment of the sound levels is observed. A lower noise reduction is found for the latter. The opposite is observed for the positive angle of attack case ($\alpha = 4.62°$), for which the chord-aligned serration provides noise reduction up to $St_c \approx 20$, with the highest attenuation of 5 dB at $St_c \approx 8$, whereas the camber-aligned one reduces noise only up to $St_c \approx 13$, with the maximum reduction of 5.5 dB at low frequency.

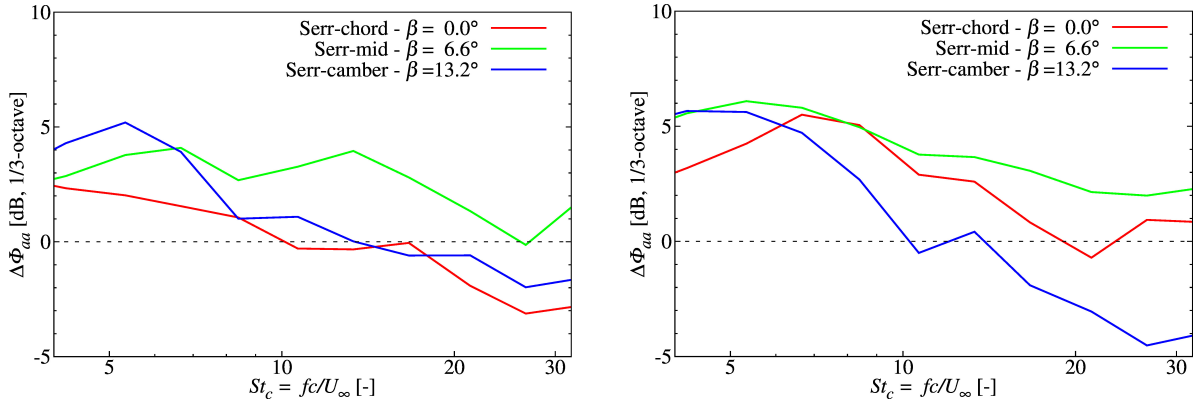

(a) *Case 6 ($\alpha = -0.88°$)* (b) *Case 7 ($\alpha = 4.62°$)*

Fig. 12 Far-field noise reduction in 1/3-octave band $\Delta\Phi_{aa}$ at (x = 0.19 m, y = 1.62 m, z = 0 m). A positive value of $\Delta\Phi_{aa}$ has the meaning of noise reduction with respect to the straight trailing-edge.

These results are in line with earlier observations from Vathylakis *et al* [26] for a NACA 65(12)-10 airfoil. They experimentally observed that flap-up positions of the serration (with respect to a camber-aligned configuration) are more favorable for broadband noise reduction, with the maximum noise reduction achieved for flap angles around 5°. Such a flap angle is similar to the $\beta = 6.6°$ cases of the present study, which also showed the best turbulent boundary-layer trailing-edge noise suppression behavior among the three examined flap angles. As previously shown in Fig. 11 and Tab. 6, the intermediate flap angle case ($\beta = 6.6°$) has only a negligible effect on the airfoil lift and drag generation. Hence, in a serrated rotor/propeller configuration, it is not expected to considerably affect the rotor performances and steady loading noise radiation, contrarily to the chord- and camber-aligned cases.

C. Far-field noise directivity

To investigate the serration flap angle influence on the far-field noise pattern, Fig. 13 depicts directivity plots of $p_{\mathrm{rms}}(\theta)/\overline{p_{\mathrm{rms}}}$ for the straight and serrated cases and for three different non-dimensional frequency ranges: $4 < St_c < 8$, $8 < St_c < 16$ and $16 < St_c < 32$. They are obtained by evaluating the acoustic pressure through a FW-H approach at 72 equally spaced microphones placed over a circular array of radius $R = 1$ m centered around the airfoil trailing-edge (Fig. 2(a)). The far-field noise levels are reported in terms of the root mean square of the acoustic pressure $p_{\mathrm{rms}}(\theta)$ normalized by the mean value $\overline{p_{\mathrm{rms}}}$ along the circular array of the straight edge case (where θ is the trailing-edge observation angle: $\theta = 0^\circ$ denotes the downstream aligned direction, whereas $\theta = 90^\circ$ denotes the suction side chord-normal view towards the trailing-edge).

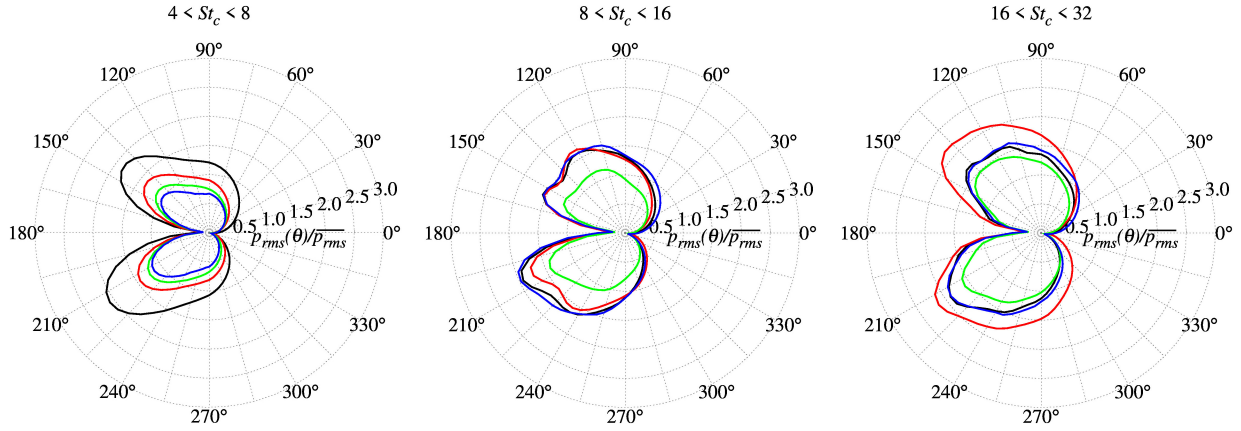

(a) *Case 6 ($\alpha = -0.88^\circ$)*

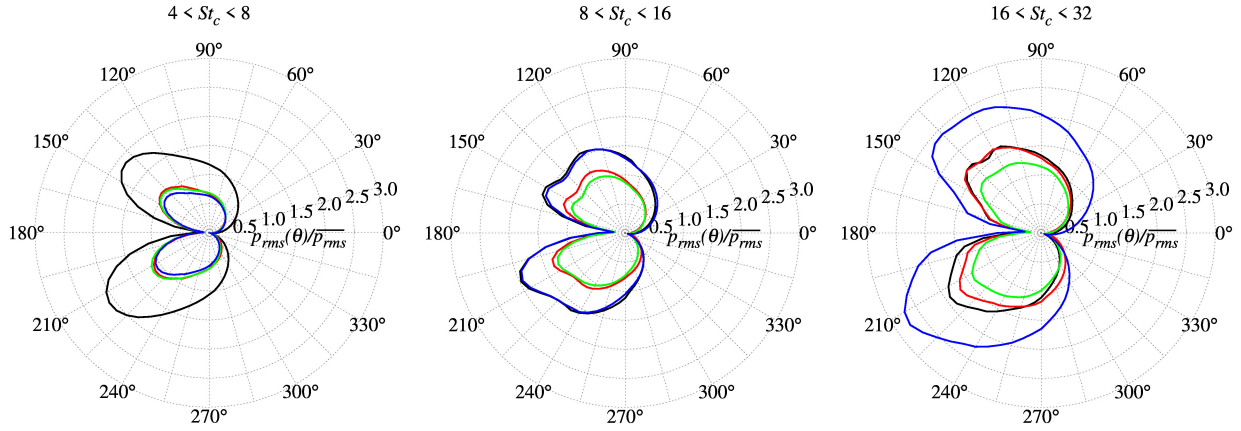

(b) *Case 7 ($\alpha = 4.62^\circ$)*

Fig. 13 Far-field noise directivity patterns for three non-dimensional frequency ranges: $4 < St_c < 8$, $8 < St_c < 16$ and $16 < St_c < 32$. Straight edge (—), Serr-chord - $\beta = 0.0^\circ$ (—), Serr-mid - $\beta = 6.6^\circ$ (—) and Serr-camber - $\beta = 13.2^\circ$ (—).

For all cases and frequency ranges examined, a non-compact dipolar pattern is observed, as expected by the value of

Helmholtz number based on the airfoil chord, which is higher than 0.5 for the lowest frequency band. As the frequency increases, the non-compact behavior becomes more significant: the dipolar pattern tends to become asymmetric with respect to the streamwise flow direction and secondary lobes are visible. For each case, most of the noise is radiated along the chord-normal and upstream directions, as known from the trailing-edge noise theory in the non-compact regime [9]. Moreover, the lobe on the pressure side results to be generally more significant than that on the suction side one for the cases examined here. Similar to what observed for the overhead microphone array, the intermediate flap angle ($\beta = 6.6°$) provides the highest noise suppression for both positive and negative angles of attack and all the frequency ranges considered, except for $4 < St_c < 8$. Moreover, for $\alpha = -0.88°$, the camber-aligned serration shows noise reduction for all directions only at low frequency ($4 < St_c < 8$), whereas the chord-aligned one also reduces noise in the mid frequency range ($8 < St_c < 16$) for some directivity angles ($195° - 270°$). At high frequency ($16 < St_c < 32$), both the chord- and camber-aligned serrations increase the noise levels compared to the straight trailing-edge for most of the observer angles. For $\alpha = 4.62°$, the camber-aligned serration reduces noise at low frequency ($4 < St_c < 8$), while increases it at high frequency ($16 < St_c < 32$) for all directions. A similar far-field noise directivity to that of the straight edge is observed at mid-frequency ($8 < St_c < 16$). A better noise suppression behavior is shown by the chord-aligned serration, which manifests noise reduction also at mid frequency for all directions, and at high frequency for some directivity angles ($180° - 270°$). Finally, it is interesting to note that the serration flap angle not only alters the amount of noise reduction or increment, but also the overall orientation of the non-compact dipole, with the two lobes that tend to be tilted along the direction perpendicular to the serration chord.

D. Serrated trailing-edge scattering

In this subsection, the effect of serration flap angle on the serrated trailing-edge scattering is analyzed. This analysis follows that proposed by Avallone *et al* [25] for the analysis of the scattering of sawtooth and combed-sawtooth serrations retrofitted to a NACA 0018 under zero lift conditions. The serration region, which extends from the last 2.5% of the airfoil surface up to the serration tip, is split into 10 strips, each of which is independently used to compute the acoustic signature $p'(t)$ in the far-field ($x = 0.19$ m, $y = 1.62$ m, $z = 0$ m) by means of the FW-H acoustic analogy. The strips

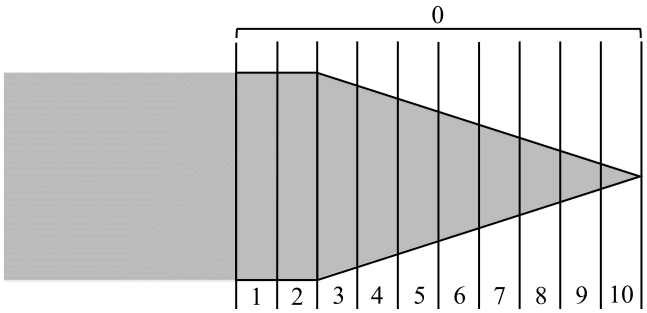

Fig. 14 Sketch of the serration surface partition for scattering analysis.

are numbered from 1 to 10 and the strip 0 is used to account for the entire serration region, as depicted in Fig. 14. The acoustic signature from each strip is used to compute the Fourier transform of the cross-correlation between strips, i.e the cross-spectral density $C_{ij}(f)$, in order to highlight constructive and/or destructive interference of noise sources distributed along the serration edge:

$$C_{ij}(f) = \int_{-\infty}^{\infty} \left[\int_{-\infty}^{\infty} p_i'(t) p_j'(t+\tau) d\tau \right] e^{j2\pi ft} dt. \tag{12}$$

The results from the cross-spectral density analysis are further integrated over the three frequency bands considered so far and presented in Fig. 15 and Fig. 16 for $\alpha = -0.88°$ and $\alpha = 4.62°$, respectively. In Figs. 15 and 16, the colored inner matrix shows the magnitude of cross-spectral density $|C_{ij}|$ between the i-th and j-th strips normalized by the magnitude of the auto-spectral density of the entire serration region $|C_{00}|$. This matrix is symmetric by definition. Therefore, its main diagonal represents the magnitude of the auto-spectral density of the contribution from the i-th strip. The outer grey matrix represents the values of $\cos(\phi_{i0})$, where ϕ_{i0} is the phase angle of the cross-spectral density C_{i0} between the i-th strip and the entire serration region. If C_{i0} is close to 1, the contribution of the i-th strip is in phase with that of the overall serration, thus leading to constructive interference. The opposite situation occurs for C_{i0} close to -1. It should be pointed out that this analysis would, in principle, neglect the constructive and/or destructive interference between the different serration teeth. However, as previously mentioned, it has been verified that the spanwise coherence length upstream the serrated trailing-edge is not significantly affected by the presence of the serration. Therefore, considering Fig. 9 and that $s = 2\lambda$, it can be inferred that the pressure coherence length is smaller than the serration wavelength λ and no coherent interference is expected between the different serrations. The spanwise coherence length averaged along the serration will be shown in Sec. V.F to further support this point. Finally, it is worth mentioning that each serration strip might contain scattered noise from the other strips due to the compressible nature of the LBM scheme. However, its contribution to the far-field noise is expected to be a small compared to that associated to the hydrodynamic pressure fluctuations.

The magnitude of the cross-spectral density shows that, regardless of the flap angle and airfoil incidence, the dominant sources of noise are mainly located at the root of the serration. However, whilst at low frequency the main noise sources are confined to the very beginning of the serration, they are much more distributed along the serrated edge as the frequency increases. This is consistent with the findings of Avallone *et al* [25] for a symmetric airfoil retrofitted with sawtooth serrations at zero flap angle and angle of attack. On the other hand, the phase angle results of the cross-spectral density tend to partially differ from those of the above mentioned study. Indeed, they found that the scattered waves at the central part of the serration destructively contribute to the low-frequency far-field noise radiated by the entire serration region [25]. In the present study, none of the strips shows a strong out-of-phase noise radiation (i.e. $\cos(\phi_{i0}) < -0.5$) and only some moderate phase differences between the scattered waves are found. This aspect is

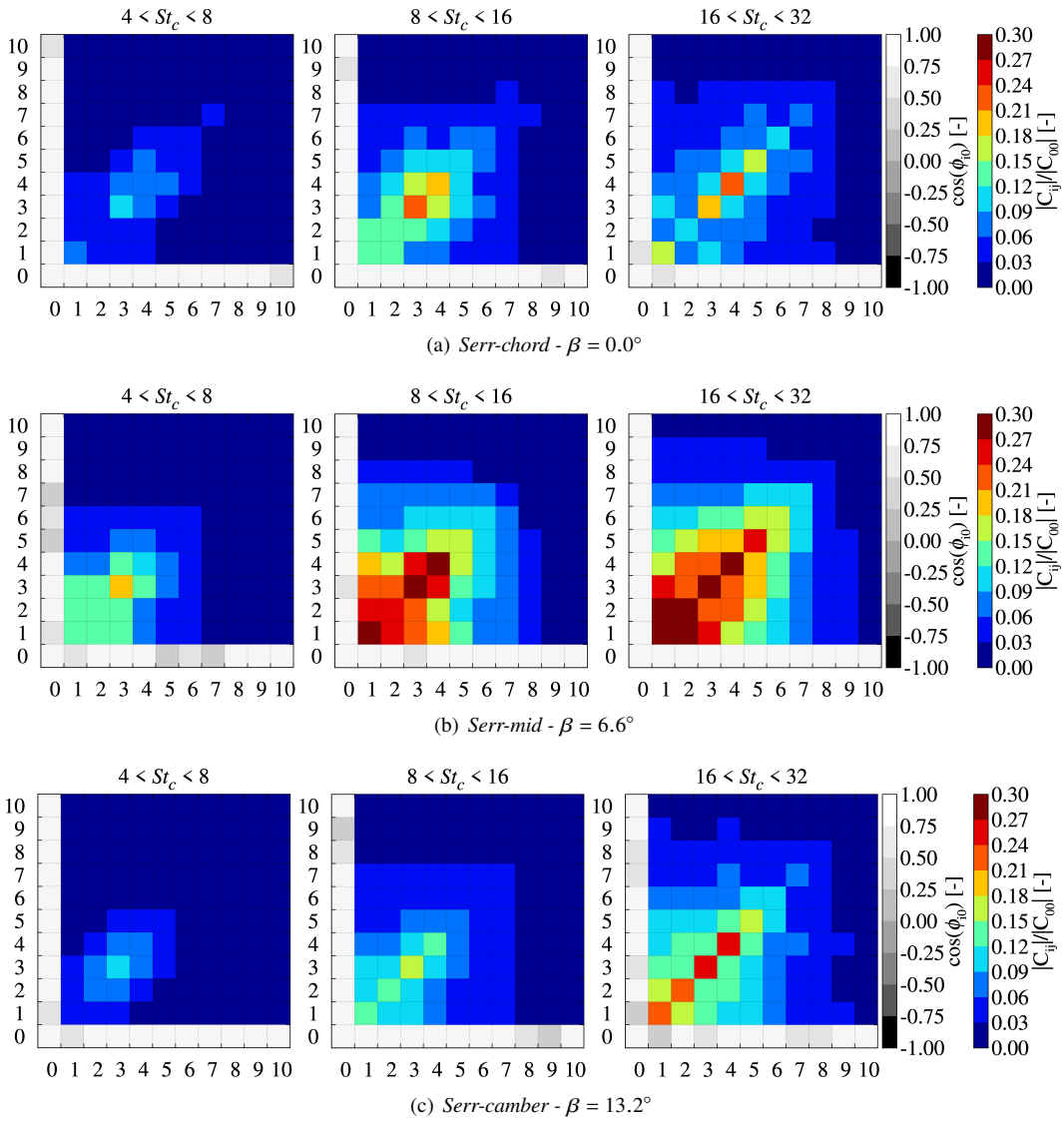

(a) *Serr-chord* - $\beta = 0.0°$

(b) *Serr-mid* - $\beta = 6.6°$

(c) *Serr-camber* - $\beta = 13.2°$

Fig. 15 Normalized cross-spectral density matrix (colored scale) between the different serration strips and phase information (grey scale) with respect to the overall serration region, case 6 ($\alpha = -0.88°$).

observed for all the angles of attack and flap angles examined here. These findings suggest that, as the serration is at incidence with respect to the flow, a lower destructive interference among the noise sources distributed along the serrated edge is promoted compared to zero incidence serrations, thus resulting in a lower noise suppression effectiveness of the serration itself. Interestingly, for the shallow negative angle of attack case ($\alpha = -0.88°$), the mid-aligned serration (Fig. 15(b)) shows more uniform values of the auto-spectral density, as well as larger phase differences between the waves scattered from the noisiest strips and the overall serration region compared to the chord- and camber-aligned ones (Figs. 15(a) and 15(c), respectively). These aspects are responsible of a larger noise reduction [25, 58]. Similar results are observed for $\alpha = 4.62°$ (Fig. 16), although, for this angle of attack, also the chord-aligned serration shows quite distributed noise sources along the serrated edge (Fig. 16(a)) and some phase differences between the acoustic

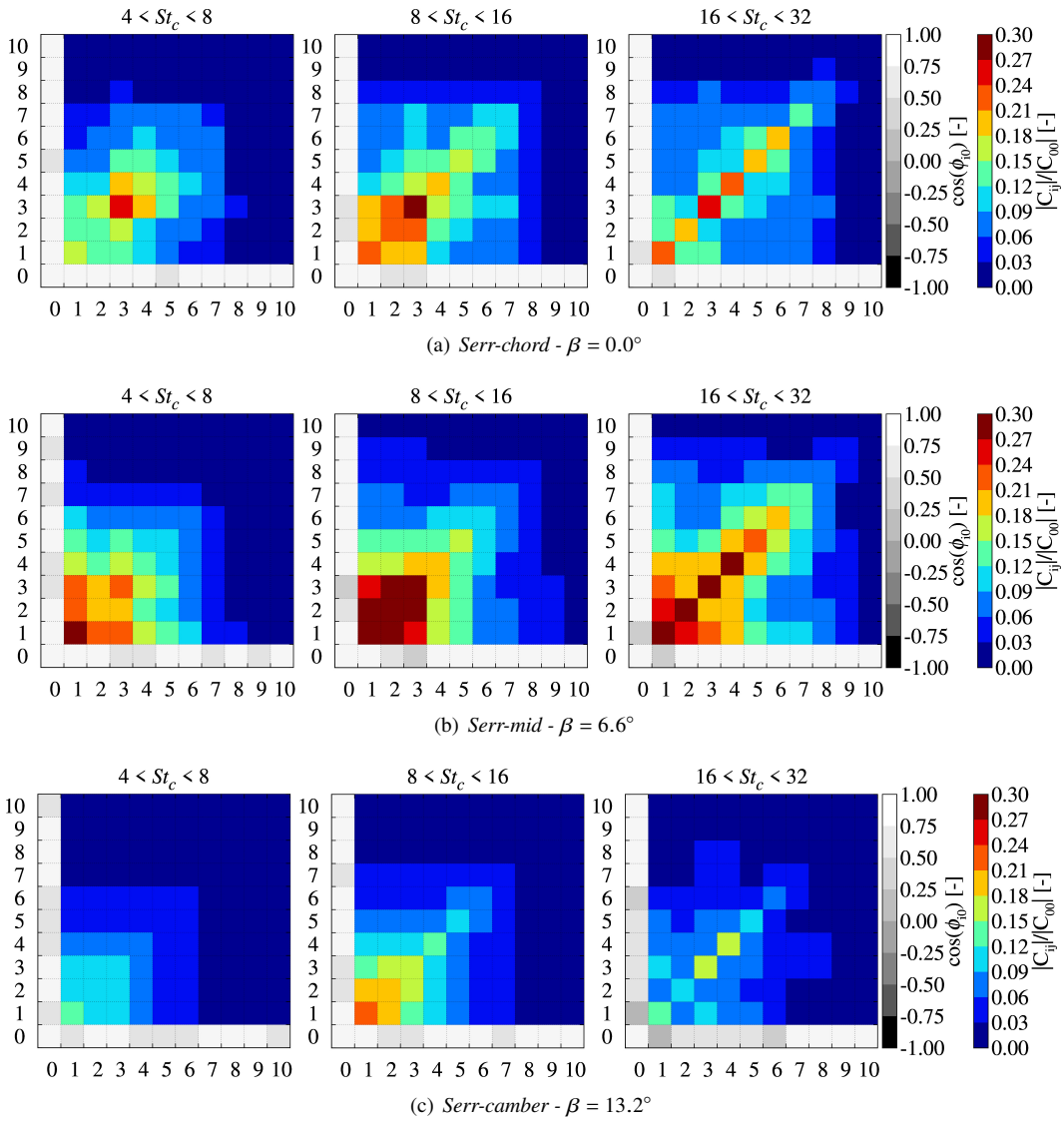

(a) *Serr-chord* - $\beta = 0.0°$

(b) *Serr-mid* - $\beta = 6.6°$

(c) *Serr-camber* - $\beta = 13.2°$

Fig. 16 Normalized cross-spectral density matrix (colored scale) between the different serration strips and phase information (grey scale) with respect to the overall serration region, case 7 (α = 4.62°).

signatures radiated from the noisiest strips and the overall serration.

E. Mean flow around the serrated trailing-edge

The far-field noise analysis showed that for both angles of attack considered in this study, the serration mounted at an intermediate flap angle between the chord- and camber-aligned configurations manifested the highest noise reduction. Moreover, the analysis of the scattering behavior of the serration showed that, although the noise sources are mainly localized at the serration root for each flap angle, they are more distributed along the serrated edge for the $\beta = 6.6°$ case. This might be caused by a modification of the mean flow organization for different serration flap angles. Earlier studies conducted by Howe [11], Chong & Vathylakis [17], Arce-León *et al* [27] and Avallone *et al* [25] indicated that the flow

alignment with respect to the serrated edge represents one of the driving mechanisms that positively contributes to the noise reduction. In order to verify this finding, Figs. 17 and 18 depict the time-averaged flow deflection angle φ over the serration, extracted at the closest voxels layer to the add-on surface, with near-wall streamlines superimposed. The angle φ represents the deflection angle between the undisturbed and actual (local) streamlines, and is defined as $\varphi = \tan^{-1}(\langle w \rangle / \langle u \rangle)$, where $\langle u \rangle$ and $\langle w \rangle$ are the wall-parallel (i.e. directed as x_s) and spanwise (i.e. directed as z_s) time-averaged flow velocity components, respectively. One can note that a modification of the deflection angle φ results in a change of the effective angle (i.e. the angle between the serrated edge and the local streamline) at which the turbulent structures are convected over the slanted edge.

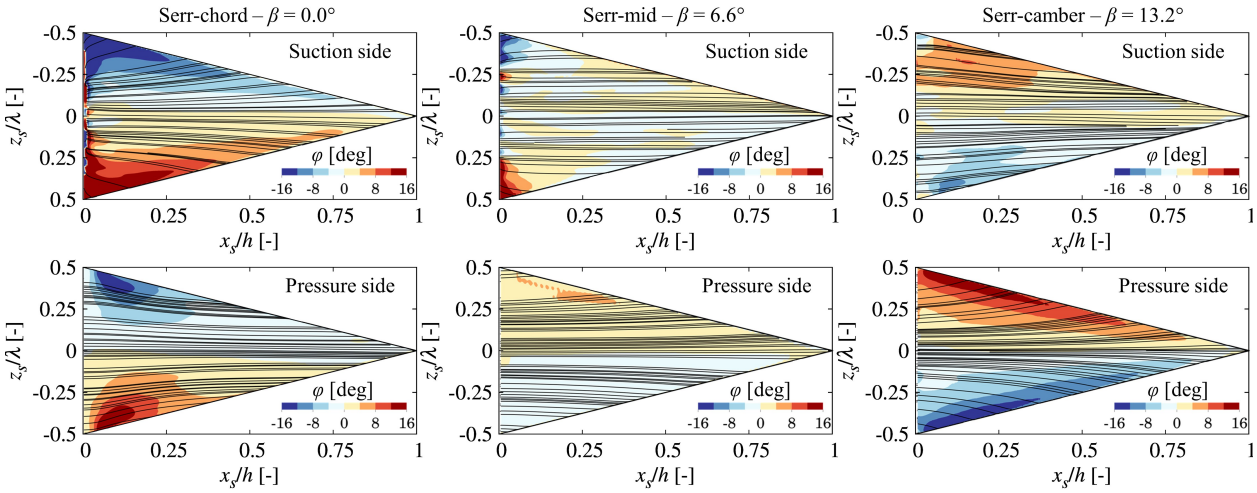

Fig. 17 Contours of time-averaged near-wall flow deflection $\varphi = \tan^{-1}(\langle w \rangle / \langle u \rangle)$ and streamlines, case 6 ($\alpha = -0.88°$).

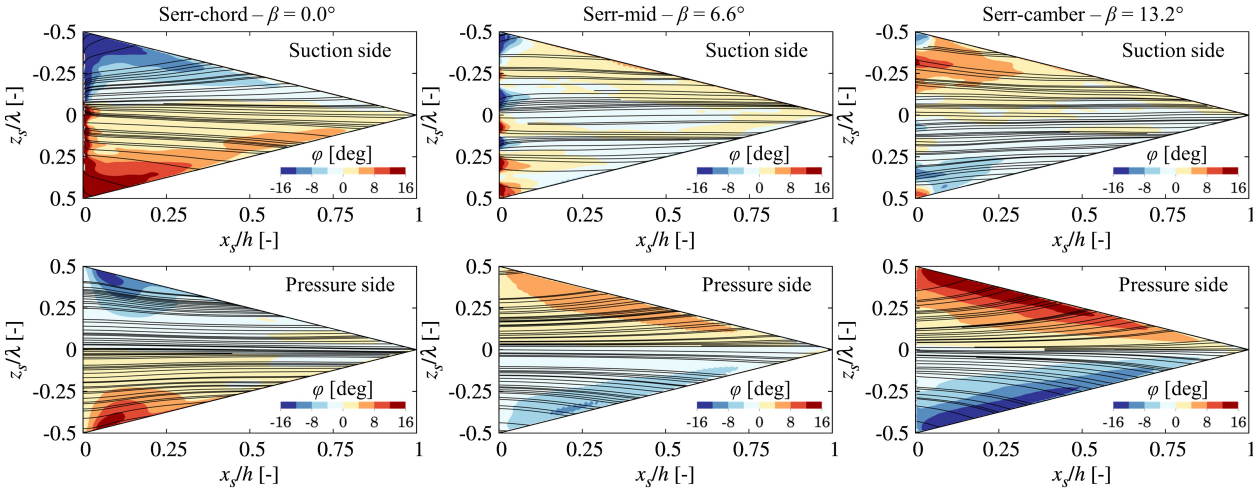

Fig. 18 Contours of time-averaged near-wall flow deflection $\varphi = \tan^{-1}(\langle w \rangle / \langle u \rangle)$ and streamlines, case 7 ($\alpha = 4.62°$).

For the shallow negative angle of attack case (Fig. 17) and flap angle $\beta = 0.0°$, the flow exhibits a pronounced outward motion (i.e. from the centerline of the serration towards the serration edge) on the suction side at the root of the serration. On the pressure side, a weaker inward motion (i.e. from the serration edges towards the centerline of the serration) is visible. The opposite situation occurs for the camber-aligned serration ($\beta = 13.2°$), whereas the $\beta = 6.6°$ case shows an intermediate condition with respect to the chord- and camber-aligned configurations, with the near-wall streamlines mostly aligned with the streamwise direction. These aspects can be related to the overall noise reduction performance of the intermediate configuration: the outward flow motion enhances the efficiency of the noise scattering of the sources on the serrated edge, as the streamlines are more perpendicular to the local edge (i.e. larger effective angle). Moreover, for the chord and camber aligned cases, the large outward flow motion near the root, on the suction side for $\beta = 0.0°$ and on the pressure side for $\beta = 13.2°$, might explain why the strongest noise sources are more localized towards the root for these angles, whereas are more distributed along the edge for $\beta = 6.6°$. Similar considerations can be argued for the positive angle of attack case (Fig. 18). However, although the level of misalignment between the local streamline and the serrated edge considerably influences the efficiency of the noise radiation, it cannot be used to completely explain the noise reduction, as pointed out by Arce-León *et al* [19]. This might explain why the camber-align serration ($\beta = 13.2°$) performs similarly to (for $\alpha = 4.62°$) or even better then (for $\alpha = -0.88°$) the intermediate one ($\beta = 6.6°$) at low frequency, despite the large flow deflection of the former on the pressure side.

Figure 19 depicts the time-averaged streamwise vorticity component $\langle \omega_x \rangle$ for various combinations of angles of attack and flap angles at five different uniformly spaced cross-flow planes, spanning from the root to the tip of the serration. In addition, mean-flow streamlines around the serration tooth are also shown. Streamwise contra-rotating vortices generated around the slanted edges are visible for each case. The circulation associated to these horseshoe vortices tends to be more affected by the serration flap angle than the airfoil angle of attack, as expected, due to the larger values of the former compared to the latter. For the chord-aligned serration, these vortex pairs reveal a downwash motion between the serrations and an upwash motion on the tooth itself. This effect occurs for both $\alpha = -0.88°$ and $\alpha = 4.62°$, but it is more significant for the former. The opposite situation takes place for the mid- and camber-aligned serrations, although it turns out to be much more evident for the positive angle of attack case ($\alpha = 4.62°$). This transverse flow motion is induced by the pressure difference generated between upper and lower sides of the serrations, being the serration at incidence with respect to the incoming flow, as previously shown in Fig. 11. It is interesting to note that the intensity of the above mentioned streamwise vortices, which is more pronounced at the root of the serration, is directly correlated with the level of flow misalignment with respect to the streamwise direction observed in Figs. 17 and 18. A similar flow behavior was experimentally observed by Arce-León *et al* [19] for a NACA 0018 airfoil retrofitted with sawtooth serrations for different combinations of flap angles and angles of attack. Moreover, it is interesting to note that the configurations (Serr-chord/camber for $\alpha = -0.88°$ and Serr-camber for $\alpha = 4.62°$), which simultaneously show the larger horseshoe vortex intensity and its closer proximity to the serration tooth, are also characterized by the lower levels

of far-field noise reduction. Presumably, the more intense tri-dimensional vortex dynamics leads to additional sound generation by interacting with the surfaces, thus reducing the benefit of the serrations. From the far-field noise results (Fig. 12) and the mean-flow streamlines around the serration (Fig. 19), it can be argued that the best-suited orientation of the add-on in terms of turbulent boundary-layer trailing-edge noise reduction is that for which the serration is oriented as the mean streamlines deviation angle with respect to the tangent to the mean camber line.

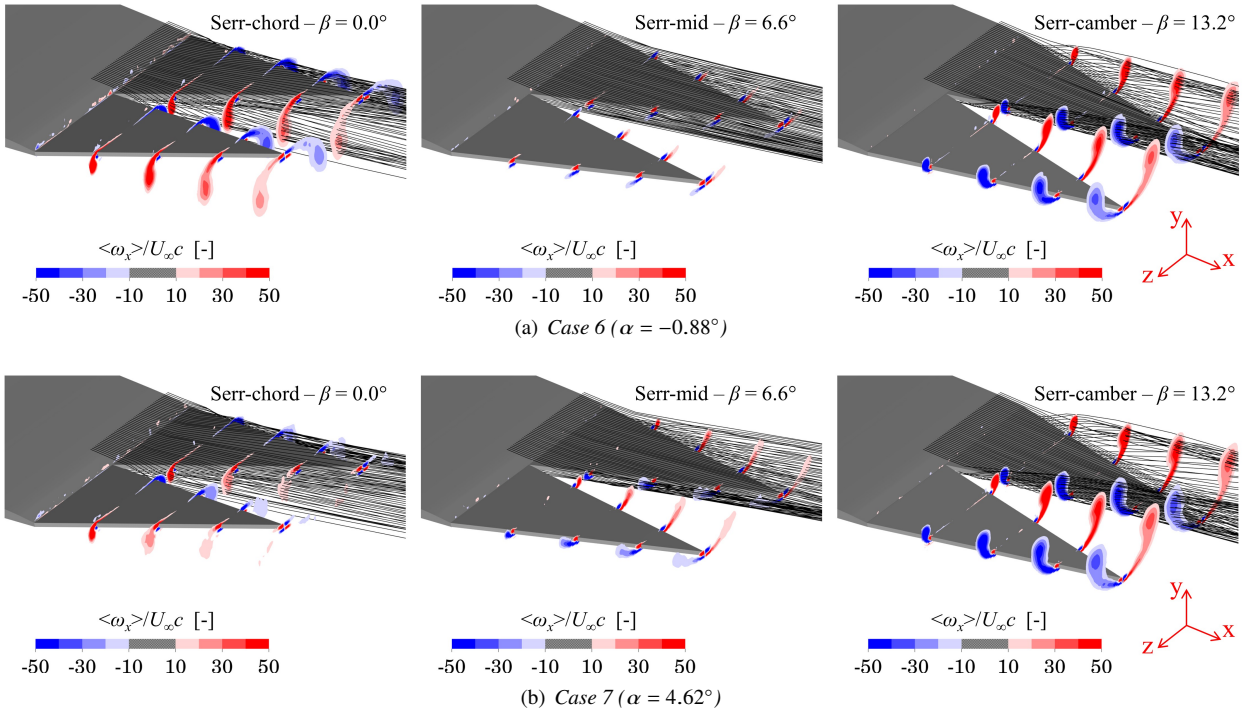

Fig. 19 Contours of time-averaged normalized streamwise vorticity component with fluid streamlines around the serrated trailing-edge (values $-10 < \langle\omega_x\rangle / U_\infty c < 10$ not shown).

F. Wall-pressure statistics along the serrated edge

As already mentioned in Sec. V.E, it is known that the level of serration-flow misalignment plays a relevant role upon the efficiency of the noise scattering of a serrated trailing-edge. However, it may not be sufficient to fully explain the resulting far-field noise [19]. Therefore, the pressure over the serrated edge is further investigated in terms of power spectral density, spanwise coherence length and convection velocity, in order to correlate the wall-pressure statistics to the radiated sound. These quantities are considered as they are those used in Amiet's trailing-edge analytical model [59]. According to this theory, higher wall-pressure spectrum, spanwise coherence length and convection velocity lead to higher far-field noise radiation for a straight trailing-edge.

Figures 20 and 21 show the wall-pressure power spectral density Φ_{pp} for $\alpha = -0.88°$ and $\alpha = 4.62°$, respectively. The wall-pressure spectra, directly obtained from the LBM simulation, are computed along the slanted edge at three

different streamwise locations ($x_s/h = 0.2$, $x_s/h = 0.5$ and $x_s/h = 0.8$) on both suction and pressure sides. For each case presented, the magnitude of the wall-pressure fluctuations tends to generally decrease from the root to the tip of the serration, confirming the observation that the intensity of the noise sources is higher in proximity of the root. Low frequencies tend to dominate the wall-pressure spectrum at the root of the serration, whereas a richer high frequency content is observed in proximity of the tip. These results are in line with the findings of Avallone *et al* [25]. In addition, for both angles of attack, the mid-aligned serration shows a much more uniform wall-pressure spectrum implying a more uniform distribution of the noise sources along the serrated edge compared to the other two flap angles. These results are consistent with the previous cross-spectral density analysis shown in Sec. V.D. For $\beta = 6.6°$, the wall-pressure fluctuations are generally smaller than (or comparable to) those of the chord- and camber aligned serrations. This suggests that another possible cause for the better noise suppression behavior of the mid-aligned serration can be ascribable to the overall lower intensity of the pressure fluctuations scattered at the serrated edge, which is related to the way the turbulent structures convect over the serrated edge as a consequence of the specific serration flap incidence.

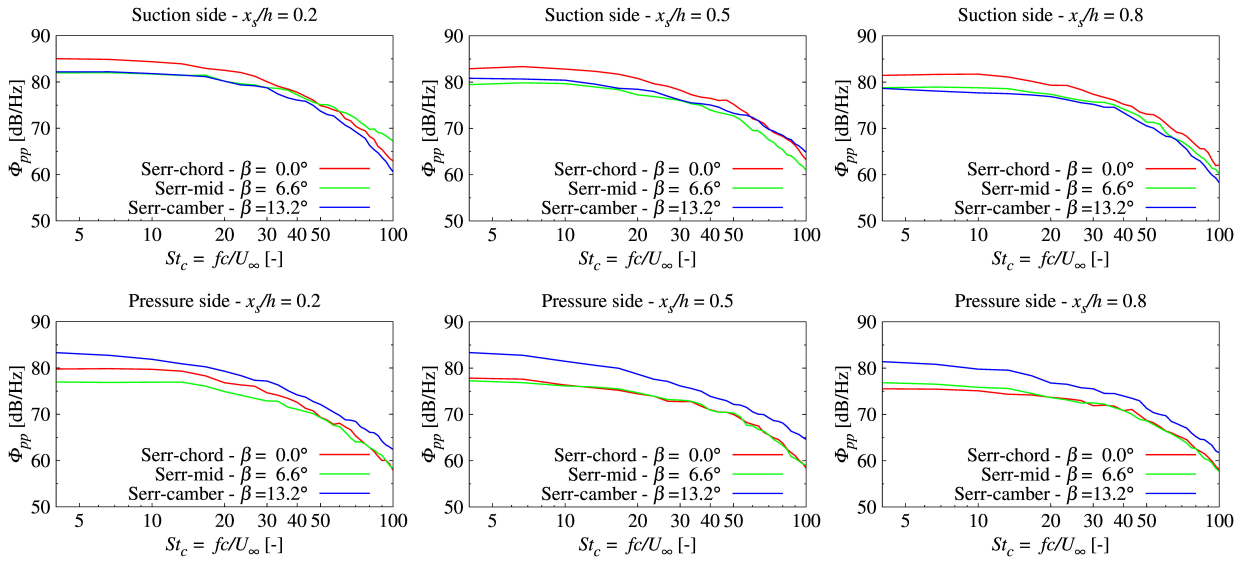

Fig. 20 Wall-pressure spectra Φ_{pp} along the serrated edge for three streamwise locations ($x_s/h = 0.2$, $x_s/h = 0.5$, $x_s/h = 0.8$) on the suction and pressure sides, case 6 ($\alpha = -0.88°$).

Since the serration flap angle might alter the way the turbulent structures are convected and distributed over the serrated edge, Figs. 22 and 23 show the spanwise coherence length l_z, the convection velocity u_c and their product $u_c l_z$ for $\alpha = -0.88°$ and $\alpha = 4.62°$, respectively. For both suction and pressure sides, the spanwise coherence length l_z is evaluated using Eq. (11) on the coherence function γ computed at three different streamwise locations on the serration (i.e. $x_s/h = 0.2$, $x_s/h = 0.5$ and $x_s/h = 0.8$) and averaging among them. Correspondingly, the convection velocity u_c is calculated along the serrated edge at the same streamwise locations on both suction and pressure sides, using the

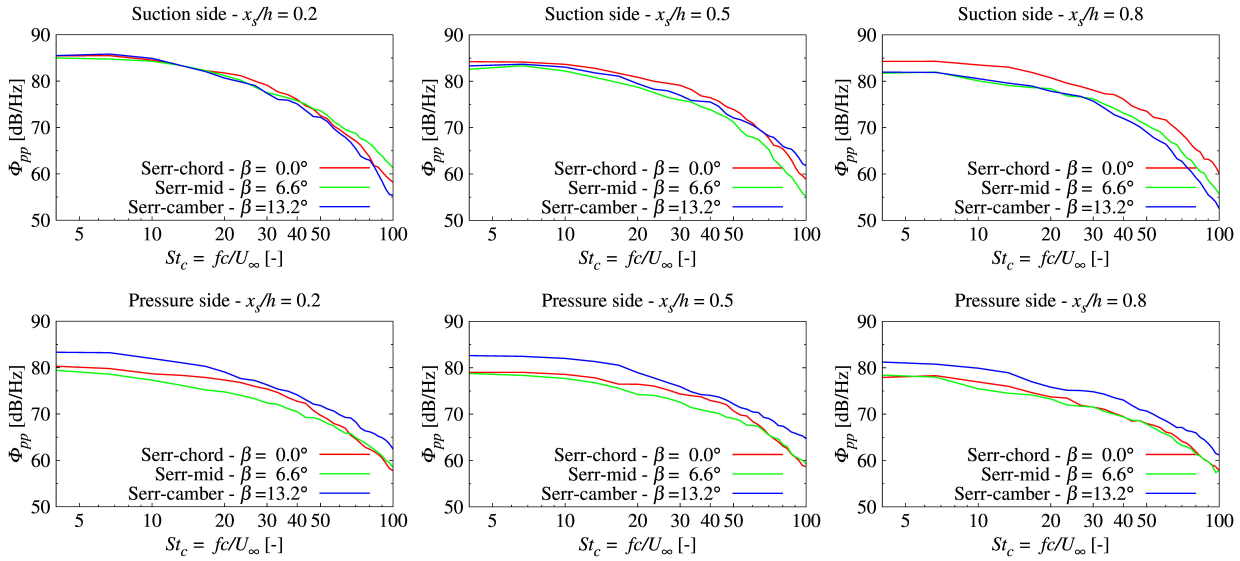

Fig. 21 Wall-pressure spectra Φ_{pp} along the serrated edge for three streamwise locations ($x_s/h = 0.2$, $x_s/h = 0.5$, $x_s/h = 0.8$) on the suction and pressure sides, case 7 ($\alpha = 4.62°$).

spectral approach proposed by Romano [60] and adopted by Chong & Vathylakis [17]:

$$u_c(f) = 2\pi\eta\left[\frac{\partial\phi}{\partial f}\right]^{-1}, \tag{13}$$

where ϕ is the phase calculated from the cross-spectral density of the wall-pressure signals between two points spaced by η along the local flow direction (i.e. the local streamline). Then, u_c is further averaged over the three streamwise locations for suction and pressure sides, respectively. This simplification of averaging l_z and u_c is carried out in order to retrieve single frequency-dependent curves to be used for comparisons among the different serration flap angles, similarly to [25]. Although not shown for the sake of conciseness, it is noted that the spanwise coherence length l_z generally decreases from the root to the tip of the serration, for each angle of attack and serration flap angle examined. For each case, it is observed that the convection velocity u_c tends to increase from the root to the tip of the serration, in agreement with previous experimental evidences [24, 27].

For a given side of the serration, similar trends of the spanwise coherence length l_z and convection velocity u_c are found for the three different flap angles between $\alpha = -0.88°$ and $\alpha = 4.62°$. For each case examined, l_z decreases as the frequency increases, showing a different decay rate depending on the flap angle and angle of attack considered. For the mid- and camber-aligned serrations, l_z generally shows higher values compared to the chord-aligned one on the suction side, while on the pressure side the chord- and mid-aligned cases show an overall larger spanwise coherence length than the camber-aligned one. This is observed for both angles of attack and is more significant for $\alpha = 4.62°$. Interestingly, for each flap angle, the different l_z curves tend to collapse on each other for $St_c > 20$. This is in agreement with previous

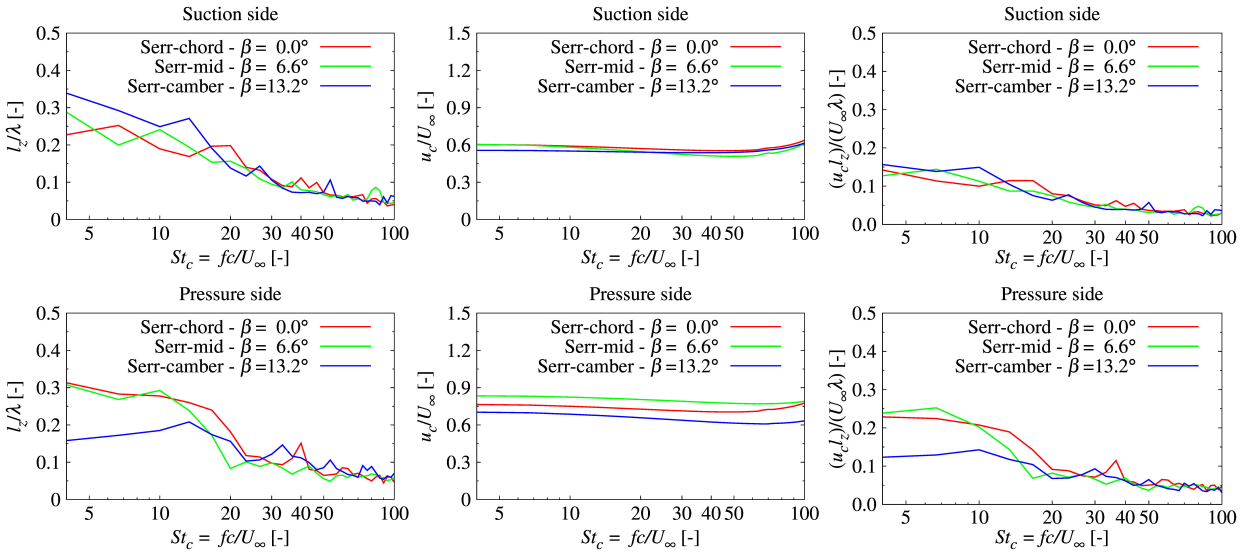

Fig. 22 Spanwise coherence length l_z (left), convection velocity u_c (center) and their product $u_c l_z$ (right) on the suction (top) and pressure (bottom) sides, case 6 ($\alpha = -0.88°$).

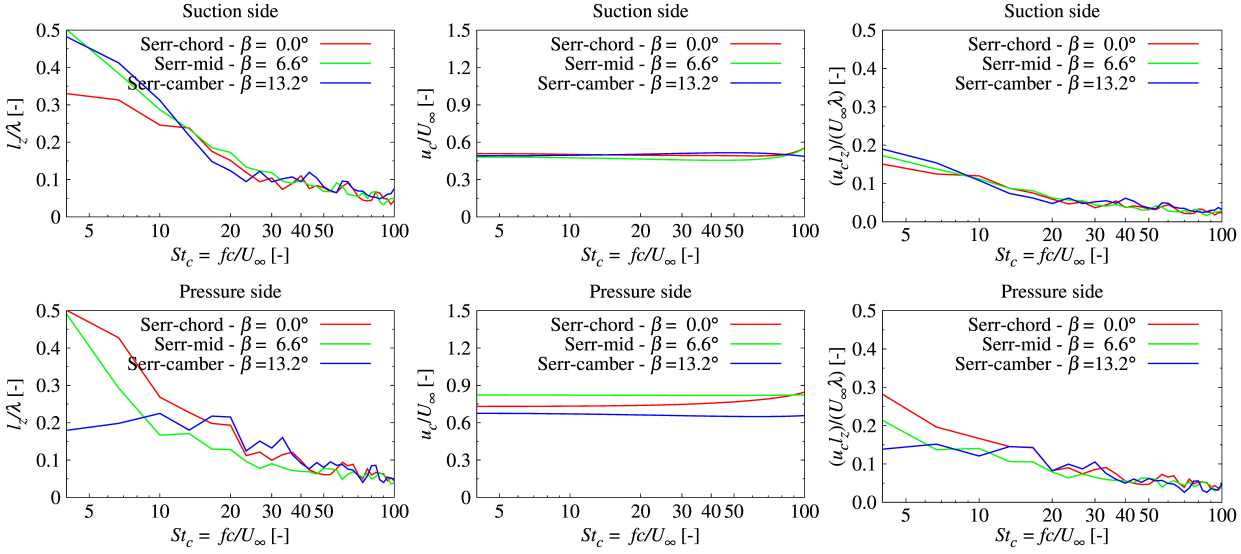

Fig. 23 Spanwise coherence length l_z (left), convection velocity u_c (center) and their product $u_c l_z$ (right) on the suction (top) and pressure (bottom) sides, case 7 ($\alpha = 4.62°$).

findings obtained by Jones & Sandberg [61] and Avallone *et al* [25], who observed that serrations do not affect the flow characteristics for high non-dimensional frequencies. A larger flow outward motion along the serrated edge results in a smaller spanwise coherence length at low frequency (and vice-versa), as shown in Figs. 17 and 22 and Figs. 18 and 23.

Regarding the convection velocity, rather constant curves of u_c with respect to frequency are found, with larger values observable on the pressure side of the serration. While on the suction side the three flap angles show very similar values of u_c, a larger scatter of the data is observed on the pressure side, with the mid- and camber-aligned

serrations showing the largest and the lowest values of u_c, respectively. The larger convection velocity for the mid- and chord-aligned cases might be associated to the presence of a more uniform flow over the serration compared to the camber aligned one, as previously highlighted in Figs. 17 and 18. Note that the non-dimensional u_c curves fall within the commonly expected values of 0.6 and 0.8 [50].

According to the straight trailing-edge noise theory [59], larger values of u_c and l_z would result in higher far-field noise levels. In contrast, for a serrated edge at zero incidence, while an increment of u_c might still result in a larger noise radiation, a higher l_z could be beneficial for noise reduction, due to the fact that it might promote destructive interference effects among scattered pressure waves within one correlation length [25, 58]. The results shown in Figs. 15 and 16 indicated that, for each angle of attack and serration flap angle, the noise sources distributed along the slanted edge are characterized by only small or moderate phase differences. This suggests that a larger spanwise coherence length would still result in a penalty in terms of noise reduction for the examined serrated cases, as for the convection velocity. For this reason, it is worth assessing the combined effect of u_c and l_z on the effectiveness of sawtooth serrations at incidence in reducing noise, by considering their product $u_c l_z$. As depicted in Figs. 22 and 23, the three different flap angles show quite similar $u_c l_z$ on the suction side for both angles of attack. Conversely, on the pressure side, the camber-aligned serration shows a smaller $u_c l_z$ at low frequency compared to the mid- and chord-aligned serrations. This aspect might explain why, at low frequencies, the camber-aligned serration showed a noise reduction higher than that associated to the other two flap angles (Figs. 12 and 13), despite the more pronounced outer motion of the flow convecting over it compared to the mid- and chord-aligned cases (as shown in Figs. 17 and 18).

In view of the above, one could conclude that the primary mechanisms by which the serration flap angle affects the trailing-edge noise reduction effectiveness of sawtooth serrations are by means of a variation of: (i) the effective angle at which the turbulent structures are convected over the trailing-edge; (ii) the convection velocity and spanwise coherence length along the serration; (iii) the intensity of the hydrodynamic wall-pressure fluctuations that are scattered along the slanted edge. Among them, the variation of the hydrodynamic wall-pressure fluctuations and the flow effective angle are believed to be the most essential mechanisms through which the serration flap angle influences the way a sawtooth serration reduces noise. This is suggested by the larger level of correlation with the far-field noise reduction showed by the modification of the aforementioned flow quantities compared to the variation of both spanwise coherence length and convection velocity.

VI. Conclusions

The flow field around a NACA 64-618 airfoil with and without serrations and its resulting turbulent boundary-layer trailing-edge noise were investigated at different airfoil angles of attack and serrations flap angles. The natural boundary-layer transition cases 6 and 7 of the AIAA BANC-V Workshop Category 1 were considered as benchmark for the validation of the computational setup for the straight trailing-edge cases. The numerical flow solution was obtained

by using the fully explicit, transient and compressible lattice-Boltzmann equation implemented in the CFD/CAA solver SIMULIA PowerFLOW®. The aerodynamic noise generated by the scattering of the hydrodynamic pressure fluctuations at the airfoil trailing-edge was estimated by using an acoustic analogy based on Farassat's formulation 1A of the FW-H equation applied to the airfoil surface.

A grid convergence study was conducted for the straight trailing-edge cases to verify the independence of the numerical results from the computational mesh. It was carried out in terms of mean pressure distribution, turbulent boundary-layer pressure and velocity statistics in proximity of the trailing-edge and far-field noise radiation for three different computational grids. It showed a good level of grid convergence for the medium resolution grid, which was consequently used for the analysis of the serration flap angle effects. Overall, the numerical results compared satisfactorily against the experimental data in terms of airfoil pressure distribution, boundary-layer profiles, far-field noise radiation and spanwise coherence length. A large over-prediction of the wall-pressure spectrum in proximity of the straight trailing-edge was observed for both cases 6 and 7. However, semi-empirical wall-pressure spectrum predictions were found to compare more favorably with the numerical results. A cross comparison between numerical results, experiments, and semi-analytical far-field noise prediction (fed with experimental wall-pressure spectra) suggested that the discrepancies observed between the numerical and experimental results could be due to a combination of factors in both simulations and experiments.

After the assessment of the computational setup for the straight trailing-edge cases, the influence of the serration flap angle on their noise reduction effectiveness was investigated. The NACA 64-618 airfoil was retrofitted with sawtooth serrations mounted at three different flap angles for both cases 6 and 7. Chord- and camber-aligned serrations, as well as an intermediate flap angle configuration were considered for each airfoil angle of attack. The analysis was carried out in terms of mean airfoil pressure distribution, far-field noise radiation, serration scattering and near-wall hydrodynamic flow topology and statistics. For the angles of attack considered, the mid-aligned serration was found to have a minimal impact on the airfoil pressure distribution and to generate only a low pressure gradient across the serration. This implies that this configuration should not considerably affect the performances and steady loading noise when retrofitted to a rotor/propeller blade. Moreover, it manifested the overall best noise suppression behavior for each angle of attack examined, except at very low frequencies, while the chord- and camber-aligned ones showed opposite noise reduction behaviors depending on the specific airfoil angle of attack. The analysis of the add-ons scattering effects showed that, for all the angles of attack and flap angles considered, no large phase differences between the acoustic waves scattered by each serration strip and the overall serration occur. This suggested that no (or only minimal) destructive interference among noise sources distributed along the serrated edge is promoted when a serration is at incidence, compared to zero incidence cases. For each case examined, it was observed that most of the noise was generated at the root of the serration, although the mid-aligned one showed a more uniform distribution of the noise sources along the slanted edge compared to the two other configurations. The serration flap angle was found to affect the far-field noise emission

primarily through a modification of: (i) the effective angle at which the turbulent structures are convected over the serrated edge; (ii) the convection velocity and spanwise coherence length along the serration; (iii) the intensity of the hydrodynamic wall-pressure fluctuations that are scattered along the serrated edge. Among them, the first and last phenomena are expected to play the most important role upon the far-field noise reduction, while the combined variation of the convection velocity and spanwise coherence length is found to influence the noise mitigation mainly at low frequency.

Acknowledgments

The authors would like to thank Andreas Fischer (Technical University of Denmark) for the provision of data that was used in this study.

References

[1] Schlinker, R. H., and Amiet, R. K., "Helicopter Trailing Edge Noise," *NASA CR-3470*, 1981. doi:https://doi.org/10.2514/6.1981-2001.

[2] Kim, Y., and George, A., "Trailing-edge noise from hovering rotors," *AIAA Journal*, Vol. 20, No. 9, 1982, pp. 1167–1174. doi:https://doi.org/10.2514/3.51176.

[3] Hubbard, H. H., "Aeroacoustics of Flight Vehicles: Theory and Practice. Volume 1: Noise Sources," Tech. rep., NASA Langley Research Center, Hampton, VA, 1991.

[4] Glegg, S., and Devenport, W., *Aeroacoustics of low Mach number flows: fundamentals, analysis, and measurement*, Academic Press, 2017.

[5] Roger, M., and Moreau, S., "Back-Scattering Correction and Further Extensions of Amiet's Trailing Edge Noise Model, Part 1: Theory," *Journal of Sound and Vibration*, Vol. 286, No. 3, 2005, pp. 477–506. doi:https://doi.org/10.1016/j.jsv.2004.10.054.

[6] Rozenberg, Y., Roger, M., and Moreau, S., "Rotating blade trailing-edge noise: Experimental validation of analytical model," *AIAA journal*, Vol. 48, No. 5, 2010, pp. 951–962. doi:https://doi.org/10.2514/1.43840.

[7] Oerlemans, S., Sijtsma, P., and López, B. M., "Location and quantification of noise sources on a wind turbine," *Journal of sound and vibration*, Vol. 299, No. 4-5, 2007, pp. 869–883. doi:https://doi.org/10.1016/j.jsv.2006.07.032.

[8] Wagner, S., Bareiss, R., and Guidati, G., *Wind turbine noise*, Springer Science & Business Media, 2012.

[9] Brooks, T., Pope, D., and Marcolini, M., "Airfoil Self-Noise and Prediction," *NASA Technical Report, Reference Publication 1218*, 1989.

[10] Ffowcs Williams, J. E., and Hall, L. H., "Aerodynamic Sound Generation by Turbulent Flow in the Vicinity of a Scattering Half-Plane," *Journal of Fluid Mechanics*, Vol. 40, 1970, pp. 657–670. doi:https://doi.org/10.1017/S0022112070000368.

[11] Howe, M. S., "Aerodynamic noise of a serrated trailing edge," *Journal of Fluids and Structures*, Vol. 5, No. 1, 1991, pp. 33–45. doi:https://doi.org/10.1016/0889-9746(91)80010-B.

[12] Howe, M. S., "Noise produced by a sawtooth trailing edge," *The Journal of the Acoustical Society of America*, Vol. 90, No. 1, 1991, pp. 482–487. doi:https://doi.org/10.1121/1.401273.

[13] Herr, M., and Dobrzynski, W., "Experimental Investigations in Low-Noise Trailing Edge Design," *AIAA journal*, Vol. 43, No. 6, 2005, pp. 1167–1175. doi:https://doi.org/10.2514/1.11101.

[14] Moreau, D. J., and Doolan, C. J., "Noise-reduction mechanism of a flat-plate serrated trailing edge," *AIAA journal*, Vol. 51, No. 10, 2013, pp. 2513–2522. doi:https://doi.org/10.2514/1.J052436.

[15] Azarpeyvand, M., Gruber, M., and Joseph, P. F., "An analytical investigation of trailing edge noise reduction using novel serrations," *19th AIAA/CEAS aeroacoustics conference*, 2013, pp. 1–17. doi:https://doi.org/10.2514/6.2013-2009.

[16] Gruber, M., Joseph, P. F., and Azarpeyvand, M., "An experimental investigation of novel trailing edge geometries on airfoil trailing edge noise reduction," *19th AIAA/CEAS Aeroacoustics Conference*, 2013, pp. 1–23. doi:https://doi.org/10.2514/6.2013-2011.

[17] Chong, T. P., and Vathylakis, A., "On the aeroacoustic and flow structures developed on a flat plate with a serrated sawtooth trailing edge," *Journal of Sound and Vibration*, Vol. 354, 2015, pp. 65–90. doi:https://doi.org/10.1016/j.jsv.2015.05.019.

[18] León, C. A., Avallone, F., Pröbsting, S., and Ragni, D., "PIV investigation of the flow past solid and slitted sawtooth serrated trailing edges," *54th AIAA Aerospace Sciences Meeting, San Diego, California*, 2016, pp. 1–15. doi:https://doi.org/10.2514/6.2016-1014.

[19] León, C. A., Ragni, D., Pröbsting, S., Scarano, F., and Madsen, J., "Flow topology and acoustic emissions of trailing edge serrations at incidence," *Experiments in Fluids*, Vol. 57, No. 5, 2016, p. 91. doi:https://doi.org/10.1007/s00348-016-2181-1.

[20] Oerlemans, S., "Reduction of wind turbine noise using blade trailing edge devices," *22nd AIAA/CEAS Aeroacoustics Conference*, 2016, p. 3018. doi:https://doi.org/10.2514/6.2016-3018.

[21] Ning, Z., Wlezien, R. W., and Hu, H., "An experimental study on small UAV propellers with serrated trailing edges," *47th AIAA Fluid Dynamics Conference*, 2017, p. 3813. doi:https://doi.org/10.2514/6.2017-3813.

[22] Halimi, A., Marinus, B. G., and Larbi, S., "Analytical prediction of broadband noise from mini-RPA propellers with serrated edges," *International Journal of Aeroacoustics*, Vol. 18, No. 4-5, 2019, pp. 517–535. doi:https://doi.org/10.1177/1475472X19859889.

[23] van der Velden, W., van Zuijlen, A., and Ragni, D., "Flow topology and noise emission around straight, serrated and slitted trailing edges using the Lattice Boltzmann methodology," *Proceedings of the 22nd AIAA/CEAS Aeroacoustics Conference, Reston, Virginia*, 2016. doi:https://doi.org/10.2514/6.2016-3021.

[24] Avallone, F., Pröbsting, S., and Ragni, D., "Three-dimensional flow field over a trailing-edge serration and implications on broadband noise," *Physics of Fluids*, Vol. 28, No. 11, 2016, p. 117101. doi:https://doi.org/10.1063/1.4966633.

[25] Avallone, F., Van der Velden, W., Ragni, D., and Casalino, D., "Noise reduction mechanisms of sawtooth and combed-sawtooth trailing-edge serrations," *Journal of Fluid Mechanics*, Vol. 848, 2018, pp. 560–591. doi:https://doi.org/10.1017/jfm.2018.377.

[26] Vathylakis, A., Paruchuri, C. C., Chong, T. P., and Joseph, P., "Sensitivity of aerofoil self-noise reductions to serration flap angles," *22nd AIAA/CEAS Aeroacoustics Conference*, 2016, p. 2837. doi:https://doi.org/10.2514/6.2016-2837.

[27] León, C. A., Merino-Martínez, R., Ragni, D., Avallone, F., and Snellen, M., "Boundary layer characterization and acoustic measurements of flow-aligned trailing edge serrations," *Experiments in Fluids*, Vol. 57, No. 12, 2016, p. 182. doi:https://doi.org/10.1007/s00348-016-2272-z.

[28] Gruber, M., Joseph, P., and Chong, T. P., "Experimental investigation of airfoil self noise and turbulent wake reduction by the use of trailing edge serrations," *16th AIAA/CEAS aeroacoustics conference*, 2010, p. 3803. doi:https://doi.org/10.2514/6.2010-3803.

[29] Fischer, A., "Experimental characterization of airfoil boundary layers for improvement of aeroacoustic and aerodynamic modeling," Ph.D. thesis, 2011.

[30] Chen, H., Chen, S., and Matthaeus, W., "Recovery of the Navier-Stokes Equations Using a Lattice-Gas Boltzmann Method," *Physical Review A*, Vol. 45, No. 8, 1992, pp. 5339–5342. doi:https://doi.org/10.1103/PhysRevA.45.R5339.

[31] Bhatnagar, P. L., Gross, E. P., and Krook, M., "A Model for Collision Processes in Gases. I. Small Amplitude Processes in Charged and Neutral One-Component Systems," *Physical Review*, Vol. 94, No. 3, 1954, pp. 511–525. doi:https://doi.org/10.1103/PhysRev.94.511.

[32] Chen, H., Teixeira, C. M., and Molvig, K., "Digital physics approach to computational fluid dynamics: some basic theoretical features," *International Journal of Modern Physics C*, Vol. 8, No. 4, 1997, pp. 675–684. doi:https://doi.org/10.1142/S0129183197000576.

[33] Launder, B. E., and Spalding, D. B., "The Numerical Computation of Turbulent Flows," *Computer Methods in Applied Mechanics and Engineering*, Vol. 3, 1974, pp. 269–269. doi:https://doi.org/10.1016/0045-7825(74)90029-2.

[34] Teixeira, C. M., "Incorporating Turbulence Models into the Lattice-Boltzmann Method," *International Journal of Modern Physics C*, Vol. 9, 1998, pp. 1159–1175. doi:https://doi.org/10.1142/S0129183198001060.

[35] Boris, J., Grinstein, F., Oran, E., and Kolbe, R., "New insights into large eddy simulation," *Fluid dynamics research*, Vol. 10, No. 4-6, 1992, p. 199. doi:https://doi.org/10.1016/0169-5983(92)90023-P.

[36] Chen, H., Teixeira, C., and Molvig, K., "Realization of Fluid Boundary Conditions via Discrete Boltzmann Dynamics," *International Journal of Modern Physics C*, Vol. 9, No. 8, 1998, pp. 1281–1292. doi:https://doi.org/10.1142/S0129183198001151.

[37] Brès, G. A., Pérot, F., and Freed, D. M., "Properties of the Lattice-Boltzmann Method for Acoustics," *AIAA Paper 2009-3395*, 2009. doi:https://doi.org/10.2514/6.2009-3395.

[38] Brès, G. A., Pérot, F., and Freed, D. M., "A Ffowcs Williams-Hawkings Solver for Lattice-Boltzmann Based Computational Aeroacoustics," *AIAA Paper 2010-3711*, 2010. doi:https://doi.org/10.2514/6.2010-37110.

[39] Casalino, D., "An Advanced Time Approach for Acoustic Analogy Predictions," *Journal of Sound and Vibration*, Vol. 261, No. 4, 2003, pp. 583–612. doi:https://doi.org/10.1016/S0022-460X(02)00986-0.

[40] Farassat, F., and Succi, G. P., "The Prediction of Helicopter Discrete Frequency Noise," *Vertica*, Vol. 7, No. 4, 1983, pp. 309–320.

[41] Curle, N., "The Influence of Solid Boundaries upon Aerodynamic Sound," *Proceeding of The Royal Society of London A*, Vol. A231, 1955, pp. 505–514. doi:https://doi.org/10.1098/rspa.1955.0191.

[42] Howe, M. S., "Trailing Edge Noise at Low Mach-Numbers," *Journal of Sound and Vibration*, Vol. 225, No. 2, 1999, pp. 211–238. doi:https://doi.org/10.1006/jsvi.1999.2236.

[43] Drela, M., "XFOIL: An analysis and design system for low Reynolds number airfoils," *Low Reynolds number aerodynamics*, Springer, 1989, pp. 1–12. doi:https://doi.org/10.1007/978-3-642-84010-4_1.

[44] Ragni, D., Avallone, F., van der Velden, W., and Casalino, D., "Measurements of near-wall pressure fluctuations for trailing-edge serrations and slits," *Experiments in Fluids*, Vol. 60, No. 1, 2019, p. 6. doi:https://doi.org/10.1007/s00348-018-2654-5.

[45] Bhatia, J. C., Durst, F., and Jovanovic, J., "Corrections of hot-wire anemometer measurements near walls," *Journal of Fluid Mechanics*, Vol. 122, 1982, pp. 411–431. doi:https://doi.org/10.1017/S0022112082002286.

[46] Blake, W., *Mechanics of flow-induced sound and vibration*, Academic Press, 1986.

[47] Rozenberg, Y., Robert, G., and Moreau, S., "Wall-pressure spectral model including the adverse pressure gradient effects," *AIAA journal*, Vol. 50, No. 10, 2012, pp. 2168–2179. doi:https://doi.org/10.2514/1.J051500.

[48] Kamruzzaman, M., Bekiropoulos, D., Lutz, T., Würz, W., and Krämer, E., "A semi-empirical surface pressure spectrum model for airfoil trailing-edge noise prediction," *International Journal of Aeroacoustics*, Vol. 14, No. 5-6, 2015, pp. 833–882. doi:https://doi.org/10.1260/1475-472X.14.5-6.833.

[49] Corcos, G. M., "The Structure of a Turbulent Pressure Field in Boundary-Layer Flows," *Journal of Fluid Mechanics*, Vol. 18, 1964, pp. 353–378. doi:https://doi.org/10.1017/S002211206400026X.

[50] Rozenberg, Y., Moreau, S., Henner, M., and Morris, S., "Fan trailing-edge noise prediction using RANS simulations," *16th AIAA/CEAS Aeroacoustics Conference*, 2010, p. 3720. doi:https://doi.org/10.2514/6.2010-3720.

[51] Lee, S., and Shum, J. G., "Prediction of Airfoil Trailing-Edge Noise Using Empirical Wall-Pressure Spectrum Models," *AIAA Journal*, Vol. 57, No. 3, 2019, pp. 888–897. doi:https://doi.org/10.2514/1.J057787.

[52] Howe, M. S., "A Review of the Theory of Trailing-Edge Noise," *Journal of Sound and Vibration*, Vol. 61, No. 3, 1978, pp. 437–465. doi:https://doi.org/10.1016/0022-460X(78)90391-7.

[53] Lee, S., "Empirical wall-pressure spectral modeling for zero and adverse pressure gradient flows," *AIAA Journal*, 2018, pp. 1818–1829. doi:https://doi.org/10.2514/1.J056528.

[54] Wolf, W. R., and Lele, S. K., "Trailing-edge noise predictions using compressible large-eddy simulation and acoustic analogy," *AIAA journal*, Vol. 50, No. 11, 2012, pp. 2423–2434. doi:https://doi.org/10.2514/1.J051638.

[55] Christophe, J., Anthoine, J. P., and Leduc, B., "Application of hybrid methods to high frequency aeroacoustics," 2011.

[56] Palumbo, D., "Determining correlation and coherence lengths in turbulent boundary layer flight data," *Journal of Sound and Vibration*, Vol. 331, No. 16, 2012, pp. 3721–3737. doi:https://doi.org/10.1016/j.jsv.2012.03.015.

[57] Pröbsting, S., Scarano, F., Bernardini, M., and Pirozzoli, S., "On the estimation of wall pressure coherence using time-resolved tomographic PIV," *Experiments in fluids*, Vol. 54, No. 7, 2013, p. 1567. doi:https://doi.org/10.1007/s00348-013-1567-6.

[58] Lyu, B., Azarpeyvand, M., and Sinayoko, S., "Prediction of noise from serrated trailing edges," *Journal of Fluid Mechanics*, Vol. 793, 2016, pp. 556–588. doi:https://doi.org/10.1017/jfm.2016.132.

[59] Amiet, R. K., "Noise Due to Turbulent Flow Past a Trailing Edge," *Journal of Sound and Vibration*, Vol. 47, No. 3, 1976, pp. 387–393. doi:https://doi.org/10.1016/0022-460X(76)90948-2.

[60] Romano, G. P., "Analysis of two-point velocity measurements in near-wall flows," *Experiments in fluids*, Vol. 20, No. 2, 1995, pp. 68–83. doi:https://doi.org/10.1007/BF00189296.

[61] Jones, L., and Sandberg, R., "Acoustic and hydrodynamic analysis of the flow around an aerofoil with trailing-edge serrations," *Journal of Fluid Mechanics*, Vol. 706, 2012, pp. 295–322. doi:https://doi.org/10.1017/jfm.2012.254.